



Università degli Studi di Padova

DEPARTMENT OF GEOSCIENCES

Master degree in Geophysics for natural risks and resources

MASTER THESIS

**Reprocessing of 2D seismic data for the search of gas hydrates
in the Eastern Mediterranean region**

Candidate:
Agnese Chies

Thesis advisor:
Dr. Ilaria Barone

Research supervisors:
Dr. Umberta Tinivella
Dr. Michela Giustiniani

Gutta cavat lapidem non vi, sed saepe cadendo.

-Lucrezio-

Abstract

This master thesis work is focused on the reprocessing of 2D seismic data for the search of gas hydrates in the Eastern Mediterranean region. The dataset of the line MS-52 has been acquired through the reflection seismic technique in the Nile deep-sea fan in 1973. Data have been reprocessed by the use of the software Seismic Unix developed by Colorado School of Mines. The reprocessing of the data is composed by the following steps: quality control of the data, geometry assignment, noise removal, spherical divergence correction, application of filters and automatic gain control (AGC), pre-stack time migration and post-processing steps. The results show that the reflector taken into consideration is a lithological reflector and not a bottom simulating reflection (BSR) because it is continuous, it does not imitate the shape of the sea floor and it does not present an inverse polarity. Even if the BSR is not present, it is not excluded the existence of gas hydrates in the area of the MS-52 line. However, the water conditions are not favorable.

Contents

1	Introduction	7
1.1	Gas hydrates	8
1.2	Geological setting and hydrates in the Mediterranean region .	11
1.3	Reflection seismics in marine environments	14
2	Materials and methods	17
3	Processing steps	21
3.1	Data QC	21
3.2	Geometry assignment	21
3.3	Noise removal	23
3.4	Spherical divergence correction	27
3.5	Application of filters and AGC	29
3.6	Pre-stack time migration	35
3.7	Post processing	46
4	Results	51
	APPENDIX A	53
	References	57
	List of figures	59

Chapter 1

Introduction

This master thesis work presents the reprocessing of 2D MS-52 seismic line with the purpose of detecting the possible presence of gas hydrates in the Eastern Mediterranean region, in the Nile deep-sea fan. In particular, this reprocessing aims to confirm or disprove the presence of a bottom simulating reflection (BSR) in that region. **Praeg et al. (2008)** interpreted a reflector along this line as BSR by using a different processing sequence.

Gas hydrates are really important both because they constitute a big unconventional reservoir of methane and because they will play an important role in the climate change conditions. Consequently, it is necessary to understand the location of gas hydrates reservoirs and the total amount of gas that is stored inside the chemical compounds.

The software used for the reprocessing of the 2D seismic data is Seismic Unix (SU), developed by the Colorado School of Mines (**Cohen et al., 2023**).

This thesis work is organized in different chapters: "introduction" in which the gas hydrates composition, the geological setting and the gas hydrates in the Mediterranean region, and the reflection seismics in the marine environment are described; "materials and methods" in which data, materials and methods of acquisitions are described; "processing steps" (data QC, geometry assignment, noise removal, spherical divergence correction, application of filters and AGC, pre-stack time migration and post processing) that shows all the steps that constitute the processing; "result" in which the results are presented, with possible extensions for future works.

The results of this work show that the reflector interpreted as BSR by **Praeg et al. (2008)** is related to a lithological change. However, this does not exclude the presence of the gas hydrates in the area of MS-52 line. In other few regions of the Nile deep-sea fan, in fact the presence of gas hydrates has been observed.

This work also highlights how it is possible to improve the quality of old data

with the purpose of obtaining a detailed final stack section.

1.1 Gas hydrates

Gas hydrates, also known as clathrate hydrates, are solid nonstoichiometric inclusion compounds made up of water and gas molecules. The water forms several cavities (called polyhedra) that can be of different types through hydrogen bonds. The different varieties of polyhedra are identified by the nomenclature n^m , where n identifies the number of edges of the considered surface, while m stays for the number of faces (**Schicks 2022**). The main structures present in nature are 3: structure I (sI), structure II (sII) and structure H (sH) (**Figure 1.1**). Structure I is composed by 2 small cages (2 pentagonal dodecahedra: 5^{12}) and 6 big cages (6 tetrakaidecahedra: $5^{12}6^2$) in each cell unit, so there are 46 water molecules. Structure II is characterized by 16 small cages (16 pentagonal dodecahedra 5^{12}) and 8 large cages (8 hexakaidecahedra $5^{12}6^4$), so it has 136 water molecules. The structures I and II can be stabilized with cages partially filled by the gas molecules. Structure H has 3 small (3 pentagonal dodecahedra: 5^{12}), 2 medium (2 irregular dodecahedra: $4^35^66^3$) and 1 large (1 icosahedron: $5^{12}6^8$) cages, with 34 water molecules. This last type of structure is stabilized by the presence of large gas molecules and bigger ones (help gas in the dodecahedra structures). In general, for the three structures, there can be one single gas molecule for each cage or more than one in conditions of very high pressure and small molecules (**Majid and Koh 2021**);(**Schicks 2022**).

Gas hydrates form at specific conditions of high pressure, low temperature (related to the geothermal gradient), and require the presence of water and gas molecules (gas supersaturated aqueous solution). There are other parameters that influence the stability and occurrence of gas hydrates in nature, which are the pore water salinity, the sediments properties, the type of gas present into the compounds (single gas or mixture), and the presence of microorganisms (**Schicks 2022**). The zone in which we have the presence of stable gas hydrates is named Gas Hydrate Stability Zone (GHSZ) and it can change during time (**Figure 1.2**). This characteristic area is limited by the geothermal gradient in the marine sediments and by the equilibrium curve of the type of gas present in the formation. Another characteristic zone is the bottom of the area in which there are stable gas hydrates: this is the Base of the Gas Hydrate Stability Zone (BGHSZ) and it depends on the geothermal gradient. As we have said before, the salinity influences the stability of the gas hydrates: in fact, in freshwater there is an increase in stability, while in brine-rich water we can observe a reduction of it (**Cook and Portnov**

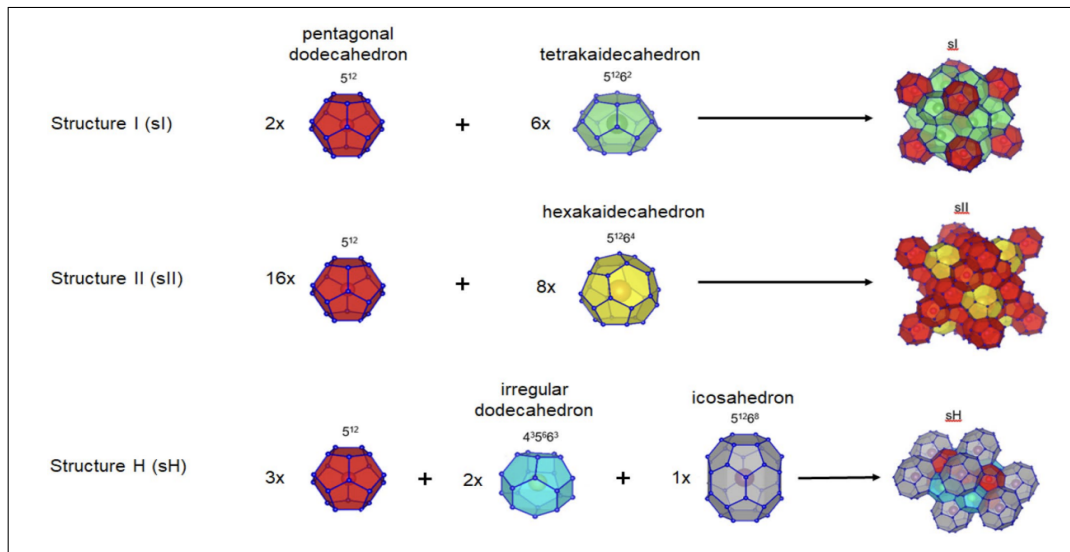


Figure 1.1: Main types of polyhedra: structures I, II and H (Schicks 2022).

2022). If gas hydrates are constituted by higher-order hydrocarbons, the GHSZ increases in thickness (Cook and Portnov 2022).

The bottom simulating reflection (BSR) in seismic data is an indicator used to detect the presence of gas hydrates into the marine sediments. This reflection represents a contrast in the acoustic impedance into the sediments caused by the presence of gas and it has an opposite polarity with respect to the seafloor reflection. In fact, the BSR divides the zone in which there is the presence of high seismic velocity gas trapped within the sediments and free gas with low seismic velocity underneath the GHSZ. There are different types of BSR (Figure 1.3):

- continuous BSR;
- discontinuous BSR;
- pluming BSR;
- clustered BSR;
- double BSR.

A continuous BSR is a laterally continuous reflection, parallel to the seafloor, with inverse polarity. Discontinuous BSRs are parallel to the bathymetry and characterized by opposite polarity but not continuous. Pluming BSRs can be continuous or discontinuous, with inverse polarity with respect to the seafloor

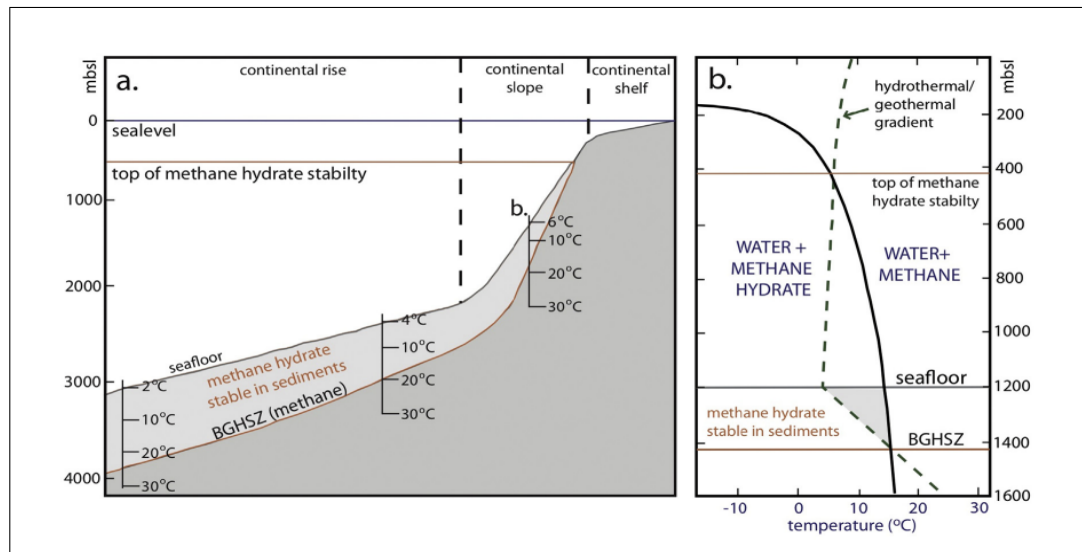


Figure 1.2: Example of the stability zone for methane hydrate, which depends on the depth and temperature (Cook and Portnov 2022).

but not parallel, due to conditions that rapidly change in space. Clustered BSRs are characterized by clustered reflections, typical of coarse-grained environments. Double BSRs are constituted by two or more reflections parallel to each other and to the seafloor, with inverse polarity (Cook and Portnov 2022).

Gas hydrates are really important for different reasons.

- They constitute a large reservoir of unconventional resources. In fact, they are common in nature and their presence has been found in deep sea sediments (95%) and in permafrost (5%) (Merey and Longinos 2018), with an estimated total amount of CH_4 sequestered by methane hydrates that goes from 10^{15} to 10^{18} m^3 at standard surface conditions (Mordis et al. 2019). They could be a large resource of energy in the future.
- Some experiments that are carried out nowadays aim to extract the methane from inside the gas hydrates and replace it with a mixture of carbon dioxide and nitrogen gas, in order to stabilize the compound and reduce the CO_2 in the atmosphere (Boswell et al. 2017).
- Gas hydrates cause some environmental concern (Obhodas et al. 2019). In fact, climate change can make the methane hydrates more vulnerable, changing the temperature and pressure conditions, causing a massive release of methane and increasing the concentration of CO_2

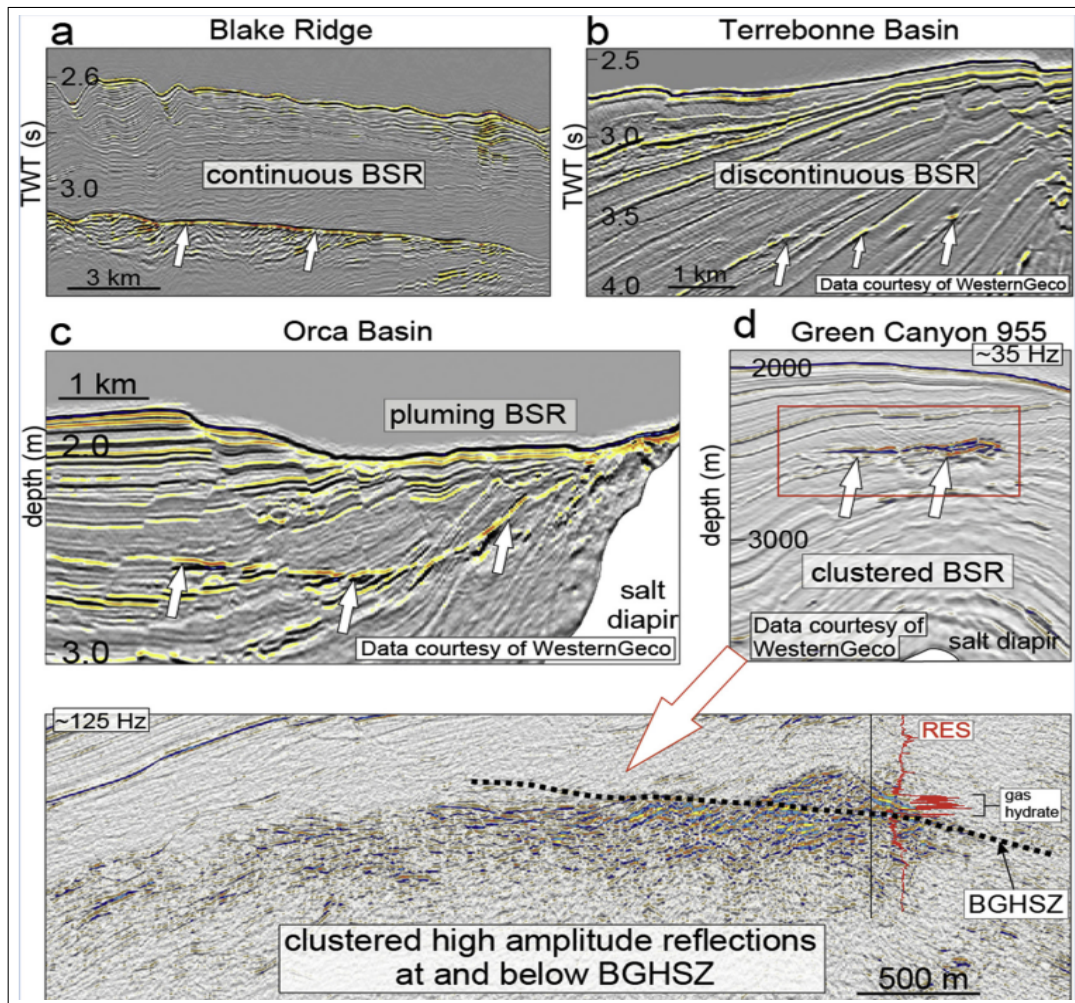


Figure 1.3: Examples of different types of BSRs (Cook and Portnov 2022).

in the atmosphere. This destabilization of methane hydrates causes the instability of continental slopes with earthquakes and tsunamis. Methane hydrates exploitation can also undermine the preservation of benthic organisms during drilling and coring operations.

1.2 Geological setting and hydrates in the Mediterranean region

The geological setting of the Nile deep-sea fan is very well described by Praeg et al. (2022). In fact, the region is composed by different areas:

western, central and eastern regions. The central area is characterized by sediments not deformed, while the western and eastern provinces are marked by an extensional fault system. Some faults are also present in the central and northern parts. Above the Messinian succession, the region presents turbiditic facies, deposits of giant-masses and mud volcanoes. The central part of the Nile deep-sea fan is characterized by pockmark-like features.

A lot of research has been conducted in order to identify the areas in the Mediterranean region where gas hydrates are present. Praeg et al. (2008) have observed a BSR on the central Nile Fan, over a depth range of 2000-2500 m, as a reflection with inverse polarity that cross-cuts stratal reflections (**Figure 1.4**). The discovery has been made through the processing of the MS-52 line data acquired by OGS in 1970s, the same line analysed in this master thesis. The processing included four steps: editing, deconvolution, stack and migration.

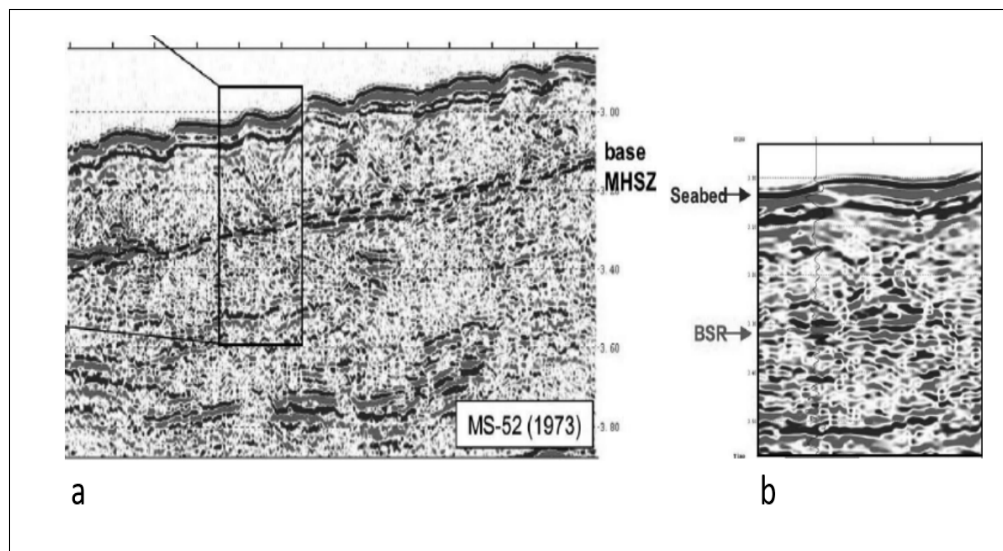


Figure 1.4: a: Reprocessed stack section of MS52 line (Praeg et al. 2008). b: Zoom of the reprocessed stack section.

In another article, Praeg et al. (2022) define the Nile deep-sea fan as a gas hydrates system of heterogeneous character. The heterogeneity of the system is due to the spatial variability of fluid expulsion from the fan. It is possible to identify a discontinuous BSR in an area of 6000 km² at water depths of 1650–2400 m. The presence of BSR has been defined using 2D and 3D exploration seismic data (**Figure 1.5**). The BSR is more visible (higher amplitude) where it cross-cuts the stratified infill of a series of fault-bound basins, while it is characterized by less amplitude but higher lateral continuity

within thick unstratified mass transport deposits (**Figure 1.6**). The presence of gas hydrates is also testified by the results that come from the well log data of the exploration wells Kg45-1 and Kj49-1, located to the West of the BSR region (**Figure 1.5** and **Figure 1.6**). The data show high resistivity values in intervals 36-75 meter thick near the base of the stability zone, but there are no seismic indications of gas in that region. **Praeg et al. (2008)** hypothesize that the discontinuity and lack of BSR is caused by higher fluid migration rates within the fan inhibiting BSR formation; the discontinuity can be attributed also to the interference created by the reflections of the stratigraphic succession of the basin. In fact, in gas venting regions the BSR was not observed, and this is probably due to higher rates of fluid migration flux. These observations are in agreement with the publication of **Majumdar et al. (2016)**, in which they declare that BSRs are not always associated with the presence of gas hydrates: in fact in many cases BSRs have no evidence of detectable gas hydrates accumulations and some gas hydrates regions are not marked by a BSR. The area analyzed by **Praeg et al. (2022)** can be subdivided into 2 regions: one characterized by the presence of discontinuous BSRs and few seafloor gas vent, while the second characterized by the lack of BSRs but with gas venting and evidence of gas hydrates in well log data. However, the total extent of the gas hydrates area is not known.

On the contrary, **Camerlenghi et al. (2022)** declared that the Mediterranean Basin is not suitable for the widespread formation and preservation of gas hydrates, due to its special features. In fact, the factors that limit the production and the stability of gas hydrates are the dense-high salinity water, the high water temperature (~ 13 °C to ~ 14 °C), the presence of high-salinity water in sediments (the salinity is always in excess of 38‰), and the presence of the low-permeability Messinian salt deposits. These factors limit the thickness of the theoretical stability zone and deepen its top surface to 1163-1391 meters water depth. **Camerlenghi et al. (2022)** built a model for the theoretical distribution of gas hydrates using the information from 44 Deep Sea Drilling Project (DSDP) and Ocean Drilling Program (ODP) boreholes, the geothermal gradients and thermohaline characteristics of water masses.

The only proved area in the Mediterranean Sea in which gas hydrates have been extracted is located in the Anaximander Mountains, in mud volcanoes. These structures are located in the Eastern Mediterranean region, to the North with respect to the Nile Fan, between Cyprus and Hellenic arcs. The total capacity of methane in Anaximander Mountains is estimated to be 2.56-6.40 km³ (**Lykousis et al. 2009**).

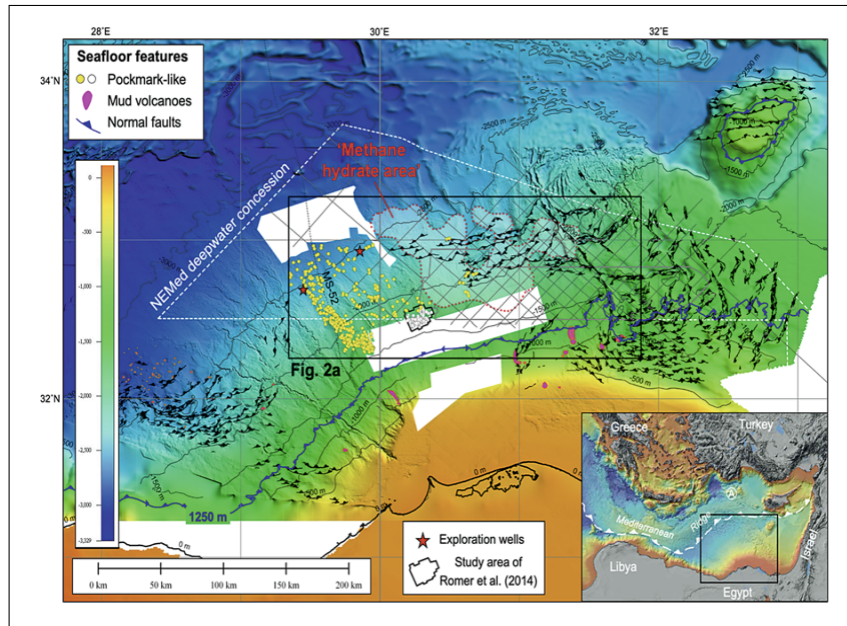


Figure 1.5: Bathymetric map with the location of the MS-52 line, the exploration wells Kg45-1 and Kj49-1 and 2D and 3D seismic exploration (**Praeg et al. 2008**).

1.3 Reflection seismics in marine environments

Reflection seismics is a geophysical method used especially for deep targets into the subsoil. This method can be used both in the land and in the sea. It consists in sending energy (elastic waves) inside the subsoil, in order to retrieve the reflected signal from underground. The reflections take place where there is a contrast in acoustic impedance (the product of density and seismic velocity of rocks). The main goal of this seismic method is to obtain a 2D or 3D image of the subsoil as a stack or migrated section, showing the main underground structures.

Focusing on marine acquisition, the seismic operations can be divided into three groups: marine, shallow water marine and ocean bottom acquisitions. Depending on the depth of the target and height of the water column, different sources and receivers types, boat models and cables for information transmission exist in order to specialize the operations. The seismic line is composed by one or more streamers of a certain length in which a defined number of hydrophones (marine acoustic sensors) are placed and these streamers are dragged by a ship, that can be a seismic ship, a catamaran or barge (depending on the operational environment). The hydrophones are

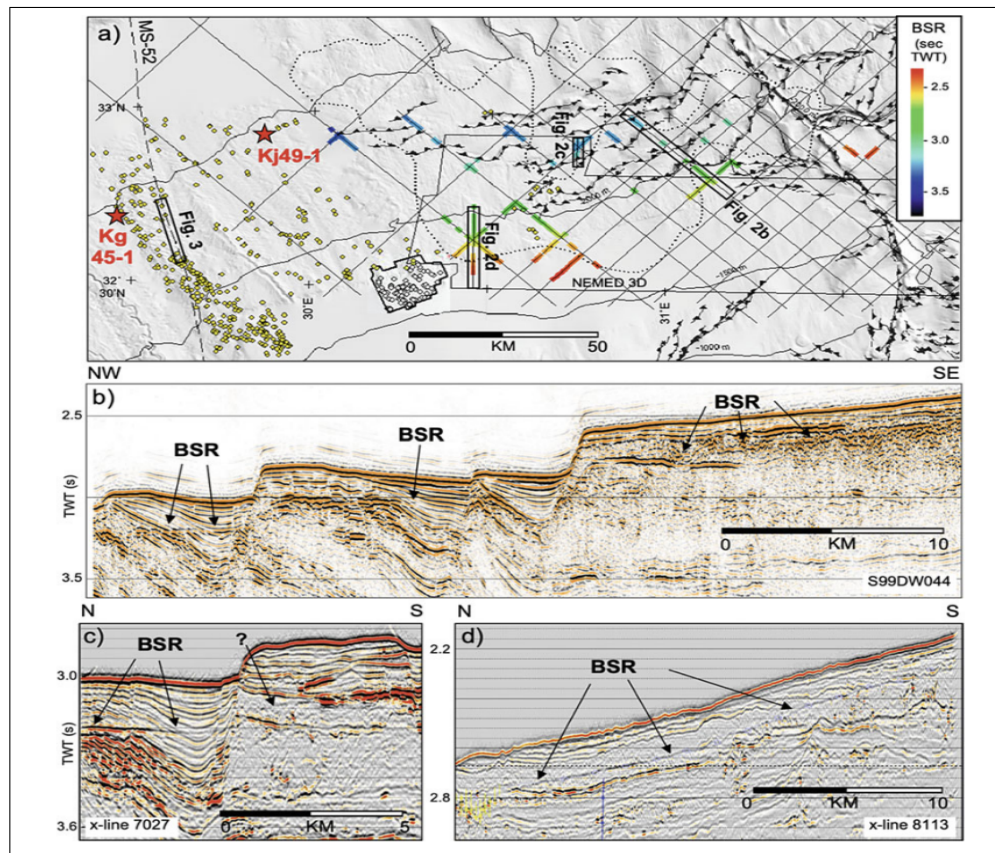


Figure 1.6: Identification of BSRs in 3D and 2D seismic profiles (Praeg et al. (2022)).

piezo-electric receivers that are sensible only to the pressure changes. Many hydrophones are placed in different streamers, that are long cables full of low-density kerosene (not conductive) able to float in the seawater. The streamers can be subdivided into analog and digital. Digital streamers digitize the signal within them and transmit it to the recorder, while analog streamers transmit the seismic amplitudes via electric signal and then it is converted to digital signal through the A/D converter. Nowadays, also solid-state streamers are used in order to avoid many technical problems of the fluid-filled streamers.

Different types of sources can be used: air guns and water guns, sparkers, boomers, chirp systems, marine vibrators. The type of source and the type of soil influence the penetration of the elastic waves into the subsoil.

During a marine acquisition, there are many factors that can create noise in the data. The noise can be subdivided in two categories: source gener-

ated noise and environmental noise, that can be coherent or random noise. The source generated noise includes air bubble, cable noise, tail buoy noise, operational noise, and source ghost (associated with receiver ghost). The environmental coherent noise includes refracted, guided and direct waves, multiple reflections, diffractions and side-sweeps. The last category (random environmental noise) includes the noise caused by marine mammals, by other boats, the powerline interference, bird noise, swell noise and spike-like noise. The processing of seismic data is composed by a set of operations that help to improve the quality of the final stack or migrated section. It aims to clean the data from all the types of noise listed before through the application of filters and muting processes. The processing also improves the temporal and spatial resolution of the data through the application of deconvolution and migration processes respectively. Basically, the processing is essential to obtain an interpretable seismic section. In this work, the processing is mainly constituted by noise removal, application of spherical divergence correction, filters and AGC, pre-stack time migration (with empirical velocity analysis), application of other filters, stack and muting processes. The empirical velocity analysis and the stack processes require the definition of the CDPs. The CDPs (common depth points) are the points on the reflector that are common for a set of traces (they constitute the common depth-point gather).

Chapter 2

Materials and methods

The acquisition of the data took place in the Eastern Mediterranean region, near the Nile fan (**Figure 2.1**). Data were acquired on the 23rd of April 1973 by OGS expedition. This line belongs to a series of lines (MS lines) recorded in the same period. The seismic line, called MS-52, is constituted by a single streamer with 24 hydrophones and it is 2300 meters long. The limited length of the streamer and the small number of sensors are due to the year of acquisition. The total length of the line is 212.8 km. The marine dataset is formed by 51096 traces, acquired through the use of 2129 shots (explosive sources) and 24 channels (hydrophones). The shot number of the part of the seismic line analysed in this master thesis starts from 2500. The sampling interval is 0.004 s and the trace length is 12 s. The average depth of the seafloor is 2590 meters. This value has been calculated by multiplying the average two-way travel time of the sea floor reflection, picked on the first trace of each shot gather, with the velocity of the water (1514, as explained in section 3.2) and dividing by a factor 2. The spacing between different sources is 100 meters, and it is equal to the spacing between different receivers. The minimum offset is 425 meters, while the maximum one is 2725 meters (**Figure 2.2**). There is no information about the type of sources and hydrophones used, but dynamite has probably been used as an explosive source. In **Figure 2.3** there is an example of a shot gather, where the traces corresponding to the 24 channels are represented in wiggle view. Both the direct wave and the sea bottom reflection are clearly visible, together with some later arrivals.

The software used for the processing is Seismic Unix, an open source seismic utilities package originally created by the Center for Wave Phenomena (CWP) at the Colorado School of Mines (CSM), used in Linux operating system (**Cohen et al., 2023**).

The main processing steps are:

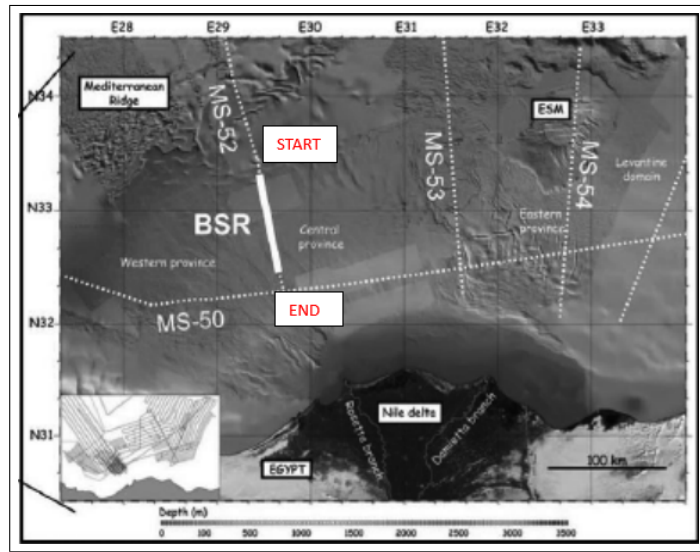


Figure 2.1: Position of the line MS52 (Praeg et al. 2008).

- Data QC (quality control);
- Geometry assignment, to add the position of the sources, receivers and the offset;
- Noise removal, where the traces affected by noise are transformed by zero amplitude traces;
- Spherical divergence correction, to compensate for the loss of energy with depth;
- Application of filters and AGC, to maintain only the frequencies characterized by the signal;
- Pre-stack time migration, to obtain a preliminary stack migrated section for interpretation. This step includes a velocity analysis;
- Post processing, that includes the application of two additional filters, the removal of the noise above the sea floor and an offset selection.

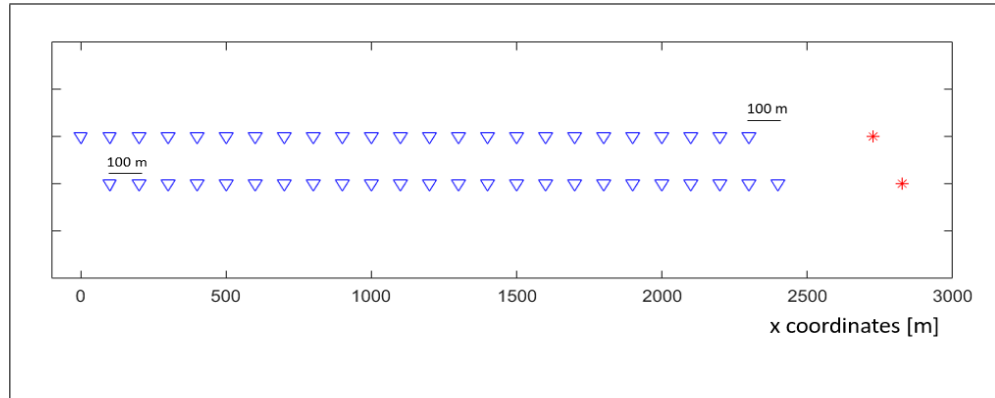


Figure 2.2: This figure represents the scheme of acquisition. In particular, two consecutive shots are visible (red stars) with the relative hydrophones (blue triangles). The spacing between two consecutive shots is 100 meters, and it is equal to the spacing between two hydrophones.

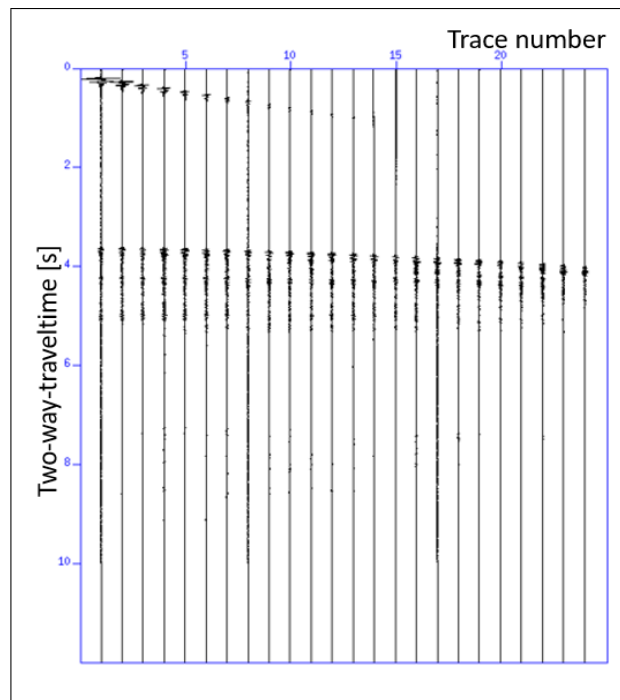


Figure 2.3: Example of a shot gather with 24 channels.

Chapter 3

Processing steps

3.1 Data QC

In the original dataset 13 shots were missing. For this reason, 13 shots characterized by zero amplitude have been added to the data (**Figure 3.1**). The missing shot numbers are: 2731, 2756, 2763, 2774, 2781, 2786, 2942, 3207, 3251, 3321, 3323, 3441 and 4617.

```
suwind < MS052.su key=ep min=2500 max=2512 > shot13.su
suzero itmax=3000 < shot13.su > shot0.su
a2b < ep.dat n1=1 > ep.bin
sushw < shot0.su key=ep infile=ep.bin > tmp
sushw < tmp key=flidr infile=ep.bin > shot0ep.su
cat shot0ep.su >> MS052.su
susort < MS052.su > MS052sorted.su ep
```

Figure 3.1: SU script used for the addition of 13 traces with zero amplitude.

3.2 Geometry assignment

The geometry (shot and receiver coordinates) has been set by the use of the script in **Figure 3.2**, using a local reference system for the 2D acquisition. The first shot is set at $x=5000$ m (arbitrarily chosen), while the coordinates of the following shots have been computed by adding a shot spacing of 100 m between each shot.

The value of the near offset was not known because it was lost in time, so it has been obtained by multiplying the first break time of the first channel and

the velocity of the direct wave in the water. The velocity of the direct wave in the water has been derived from the picking of the direct wave arrival in three different traces of many shots: in the first trace, in an intermediate trace and in one of the last traces. The picking of the first traces for different shots was also necessary to calculate the first break time that will be converted in near offset (see below). The shots that were chosen for the picking of the velocity are: 2500, 2600, 2701, 2800, 2900, 3000, 3100, 3200, 3301, 3400, 3500, 3600, 3700, 3800, 3900, 4000, 4100, 4200, 4300, 4400, 4500, 4600. However, the values of velocity for the shots 2900, 3400, 4100 and 4600 were not considered because they were too much high with respect to the expected mean value. For each shot, 3 values of velocity have been obtained, and the mean between these 3 numbers has been calculated. The values of the three velocities have been obtained with the following formulas:

$$v_1 = \frac{x_2 - x_1}{t_2 - t_1} \quad (3.1)$$

$$v_2 = \frac{x_3 - x_2}{t_3 - t_2} \quad (3.2)$$

$$v_3 = \frac{x_3 - x_1}{t_3 - t_1} \quad (3.3)$$

where x is the offset, t is the first break time, and the indexes 1, 2 and 3 refer to the first, intermediate and last trace in each gather, respectively. The final average velocity of the direct wave is 1514 m/s. The value of velocity is higher with respect to the one of the direct wave in water with normal conditions (that is 1500 m/s); this is due to the high concentration of salt in the Mediterranean Sea. The first break time has been calculated by averaging the different first break times in the first traces of the selected shots used for the estimation of the velocity. The resulting near offset value is 425 m.

Finally, the source-receiver offset has been found by considering the near offset and a spacing between receivers of 100 m. The receiver coordinates have been derived by adding the offset to the shot coordinate.

Figure 3.3 shows the common offset section with offset class 1 after the geometry assignment. A common offset section is a graphical image in which the displayed traces belong to one single offset class (a group of traces with the same offset). The dataset is divided into 24 offset classes.

```
sushw < MS052sorted.su key=sx a=5000 b=0 c=100 j=24 |  
sushw key=offset a=-425 b=-100 c=0 j=24 | suchw key1=gx  
key2=offset key3=sx b=1 c=1 > MS052geom.su
```

Figure 3.2: Script to set the geometry.

3.3 Noise removal

Another important processing step is the noise removal. The analysis for the detection of the noisy traces has been done manually for all the shots. In the first part of the section several spikes were observed, while in the last part the main disturbance consists in swell noise, probably due to rough sea conditions. A small part of the dataset also seems corrupted. All noisy traces were set to zero through the script in **Figure 3.4**. **Figure 3.5**, **Figure 3.6** and **Figure 3.7** show the three main types of noise that are present in the dataset. In this step, 1433 traces have been removed, that are the 2.8 % of the total number of traces of the dataset.

In this step of the processing, most of the noise was removed, but not all of it. In fact, in the resulting common offset section (**Figure 3.8**), a multiple is clearly visible. A multiple occurs when the seismic signal travels along the same path many times. However, this multiple has not been removed in this step because it will be deleted during the pre-stack time migration process by cutting the time at 7 seconds. This process is possible because the target of this work is shallow.

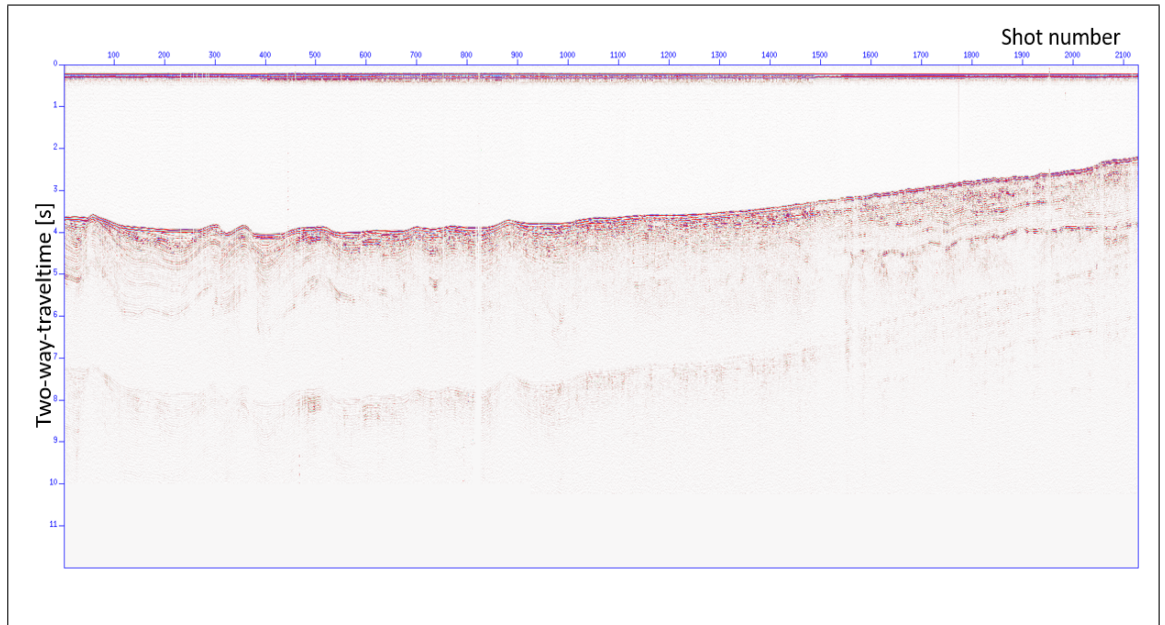


Figure 3.3: Common offset section for offset class 1 after the geometry assignment. In this figure a multiple can be identified.

```

suwind < MS052geom.su key=tracl par=accept.dat
max=0 > noise.su
suzero itmax=3000 < noise.su > noisetraces.su
suwind < MS052geom.su key=tracl par=reject.dat
min=0 > MS052geom_notraces.su
cat noisetraces.su >> MS052geom_notraces.su
susort < MS052geom_notraces.su > MS052nonoise.su
tracl

```

Figure 3.4: Script for noise removal.

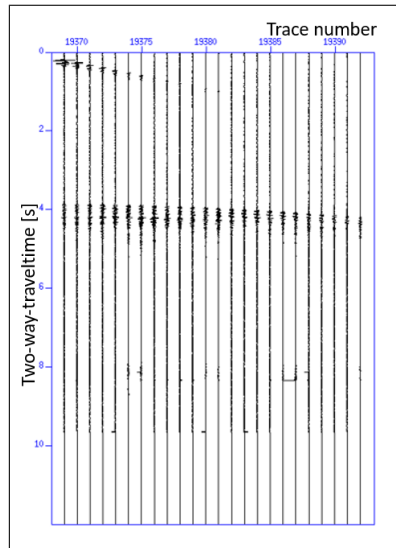


Figure 3.5: Example of a shot gather characterized by noisy spikes.

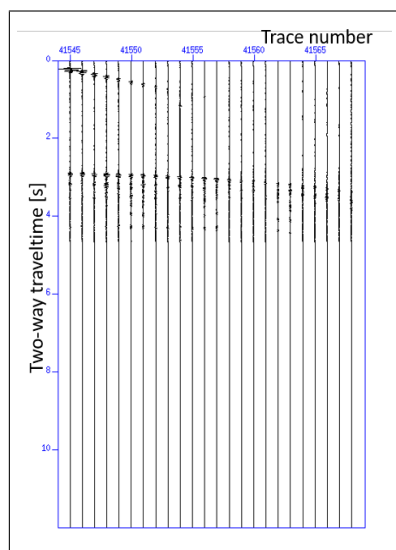


Figure 3.6: Example of a shot gather characterized by a cut below 4.8 s two-way-traveltime.

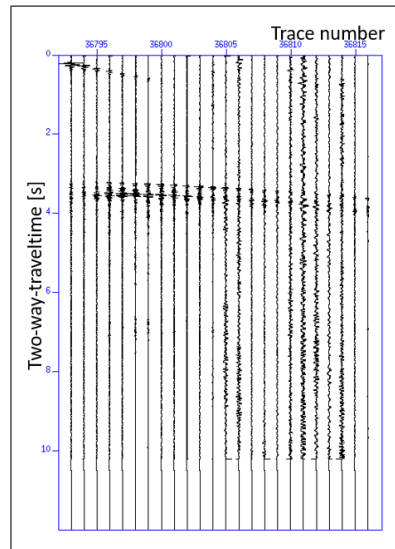


Figure 3.7: Example of a shot gather characterized by swell noise.

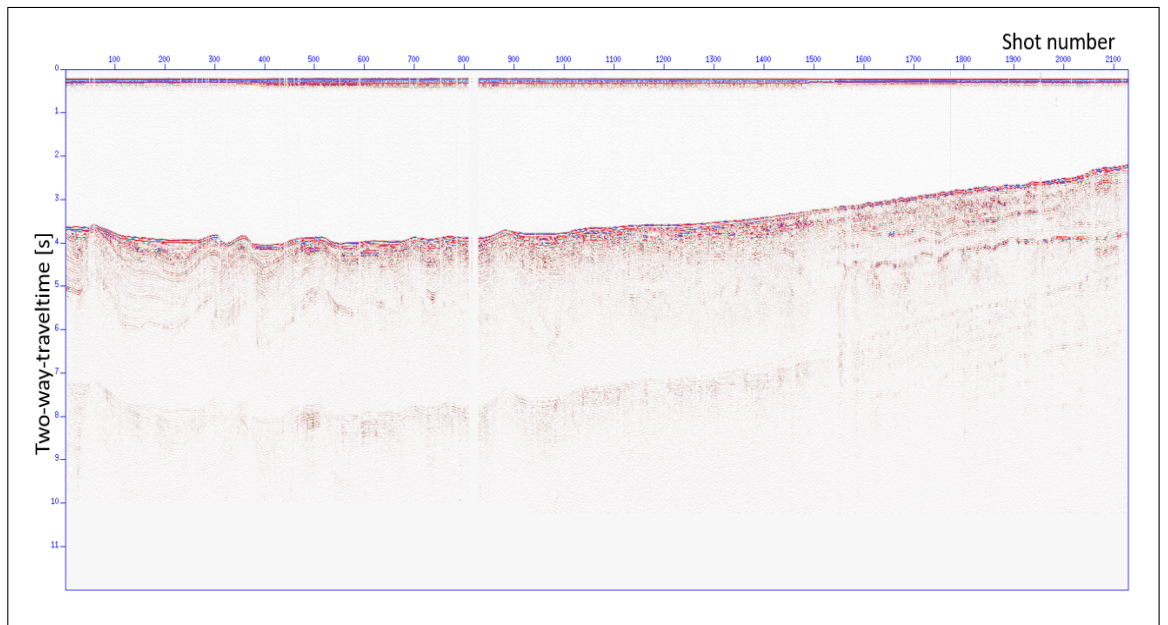


Figure 3.8: Common offset section for offset class 1, after the noise removal. In this section, it is possible to see where most of the traces have been set to zero. The section after the noise removal process presents clearer geological characteristics.

3.4 Spherical divergence correction

After the noise removal, the spherical divergence correction was applied using the script in **Figure 3.9**. The spherical divergence is the loss of energy (it decreases with $\frac{1}{r^2}$, where r is the source-receiver distance) as the wave goes into depth. The velocity used for the spherical divergence correction is the one of the direct wave in the water (1514 m/s). **Figure 3.10** shows the common offset section after the spherical divergence correction. In this section, the multiple reflection is clearer than in **Figure 3.8**.

```
sudivcor < MS052nonoise.su > MS052sphericaldiv.su  
vrms=1514.0 trms=0
```

Figure 3.9: Script for the spherical divergence correction.

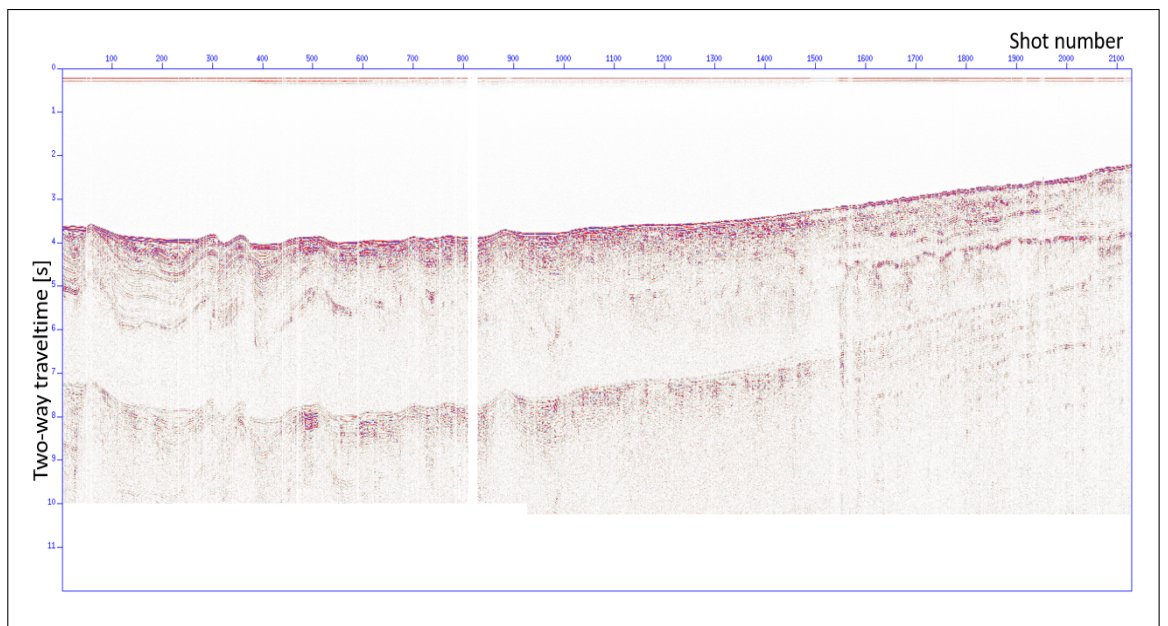


Figure 3.10: Common offset section for offset class 1, after the spherical divergence correction. After this step, the loss amplitude has been restored in depth. The multiple is more visible.

3.5 Application of filters and AGC

In this step, a band-pass filter was applied with the aim of maintaining only the frequencies in which the signal is present. This process helps to remove a part of the remaining noise from the data. Different narrow band-pass filters have been tested on the data to see their response in the common offset section, in order to choose the correct range of frequencies.

For every filter, 4 frequencies are defined: f_1 , f_2 , f_3 , f_4 . The band-pass filter is applied in the range of frequencies f_2 - f_3 . Every filter is characterized by other 2 ranges: f_1 - f_2 and f_3 - f_4 . These 2 ranges are tapers used to mitigate Gibbs' phenomenon, that occurs when there is a discontinuity in the signal related to the application of the filters. For this dataset, the sampling time is 4 ms, so the sampling frequency f_s is 250 Hz. The Nyquist frequency is $f_{NY} = \frac{f_s}{2}$. When $f_{max} > f_{NY}$ the signal is aliased, so it is important to apply some filters that have $f_{max} < f_{NY}$. For this reason, the maximum frequency for the selected filters is 120 Hz.

The filters that have been applied on the data are:

- 3-6-10-20 Hz (**Figure 3.11**);
- 3-6-16-32 Hz (**Figure 3.12**);
- 5-10-20-40 Hz (**Figure 3.13**);
- 10-20-30-60 Hz (**Figure 3.14**);
- 15-30-40-80 Hz (**Figure 3.15**);
- 20-40-50-100 Hz (**Figure 3.16**);
- 25-50-60-120 Hz (**Figure 3.17**);
- 30-60-70-120 Hz (**Figure 3.18**);
- 35-70-80-120 Hz (**Figure 3.19**);
- 40-80-90-120 Hz (**Figure 3.20**).

The Figures of the filters represent a zoom of the common offset section with common offset class 1, from trace 1600 to the last one, after the application of the AGC.

These filters have been tested on 3 different types of common offset sections:

- common offset section for offset class 1;

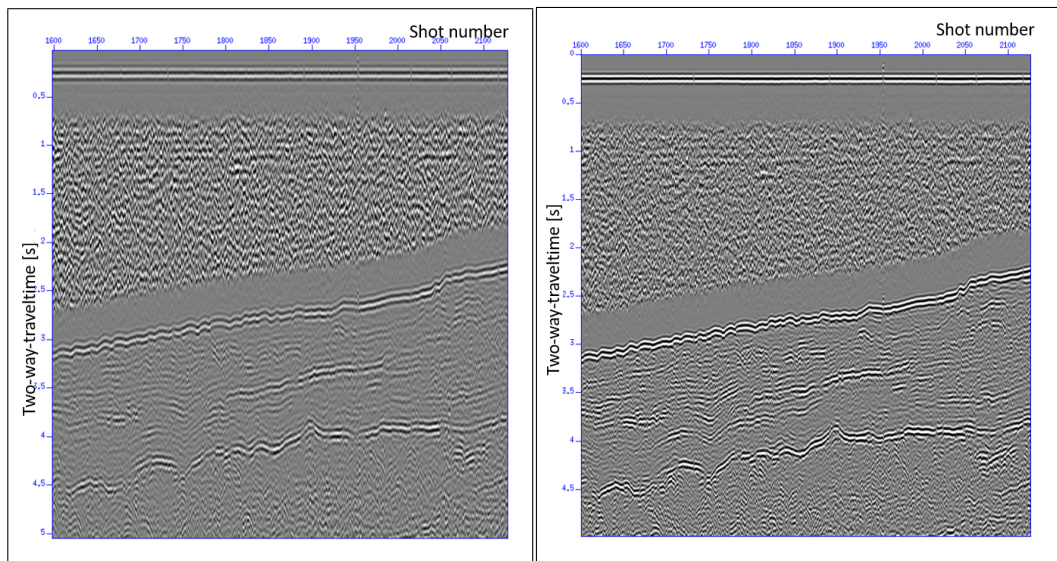


Figure 3.11: Zoom on common offset class 1 with filter 3-6-10-20 Hz. Figure 3.12: Zoom on common offset class 1 with filter 3-6-16-32 Hz.

- common offset section for offset class 12;
- common offset section for offset class 24.

As a result of these tests, the filter 3-6-90-120 Hz has been chosen (**Figure 3.21**). This range of frequencies has been set because in this interval the signal is still present.

Then, the AGC has been applied. AGC (or Automatic Gain Control) is a gain function that is applied in order to compensate for the amplitude losses with depth. AGC is applied on floating windows. Also in this case, many tests with different time window lengths took place:

- $t=0.2$ seconds
- $t=0.5$ seconds
- $t=0.8$ seconds

Also in this case, the tests have been done on 3 different filtered common offset sections (with filter 3-6-90-120 Hz):

- common offset section for offset class 1;
- common offset section for offset class 12;
- common offset section for offset class 24.

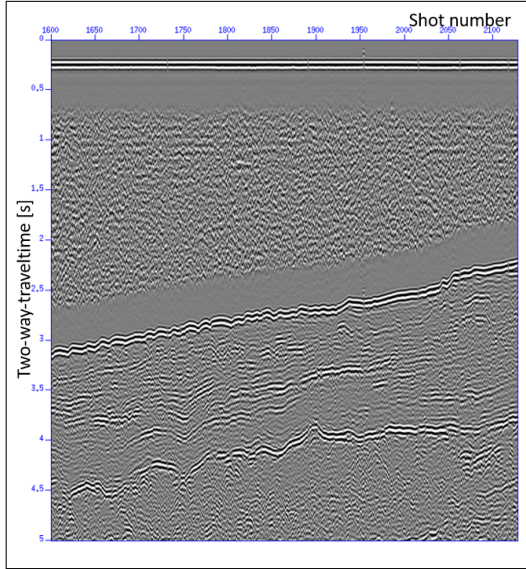


Figure 3.13: Zoom on common offset class 1 with filter 5-10-20-40 Hz.

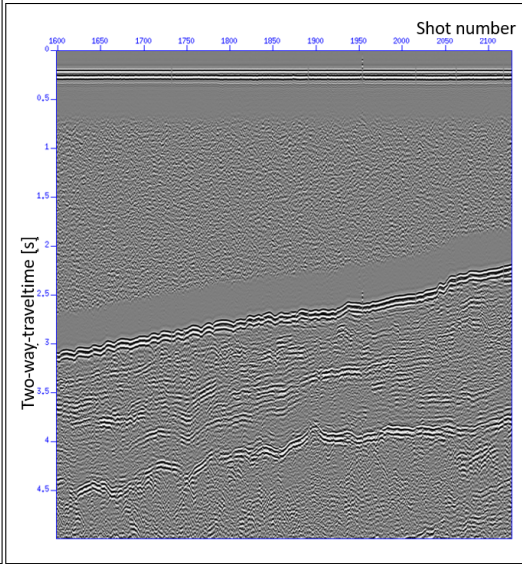


Figure 3.14: Zoom on common offset class 1 with filter 10-20-30-60 Hz.



Figure 3.15: Zoom on common offset class 1 with filter 15-30-40-80 Hz.

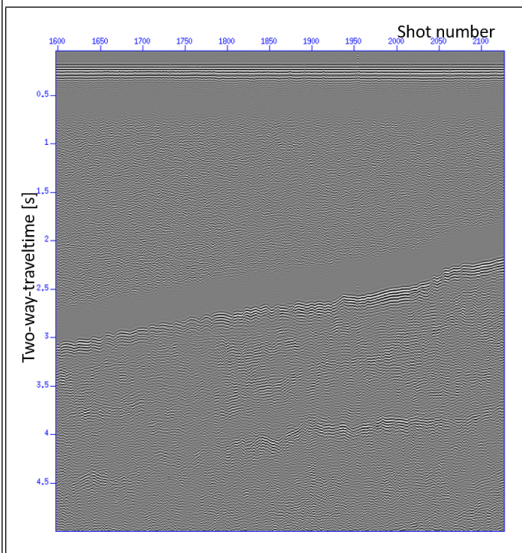


Figure 3.16: Zoom on common offset class 1 with filter 20-40-50-100 Hz.

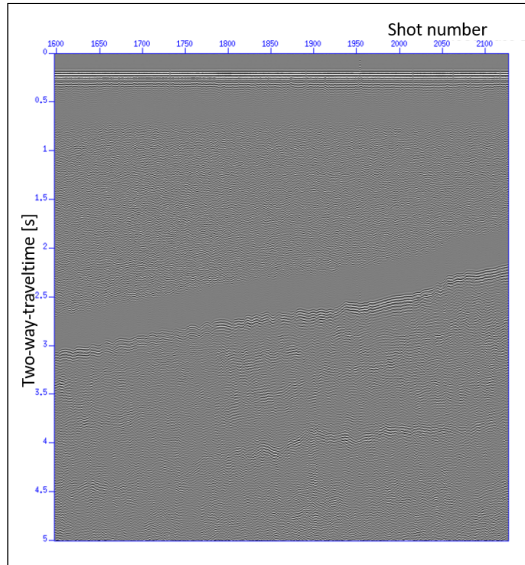


Figure 3.17: Zoom on common offset class 1 with filter 25-50-60-120 Hz.

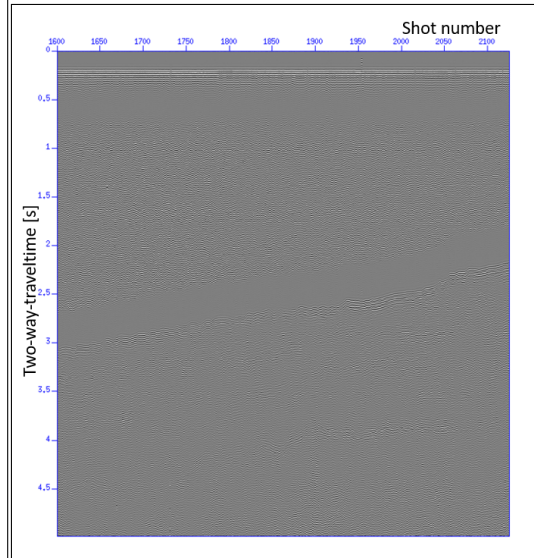


Figure 3.18: Zoom on common offset class 1 with filter 30-60-70-120 Hz.

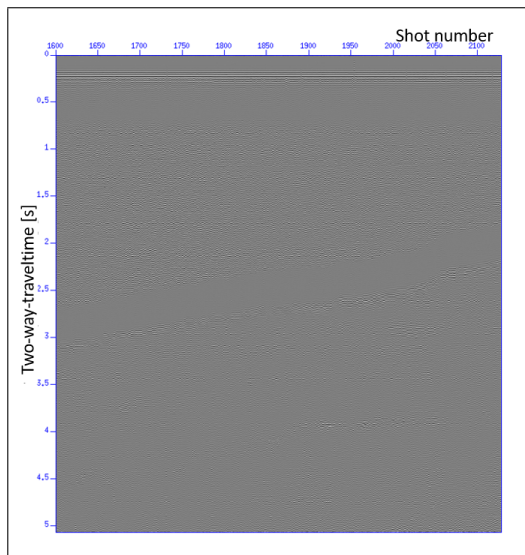


Figure 3.19: Zoom on common offset class 1 with filter 35-70-80-120 Hz.

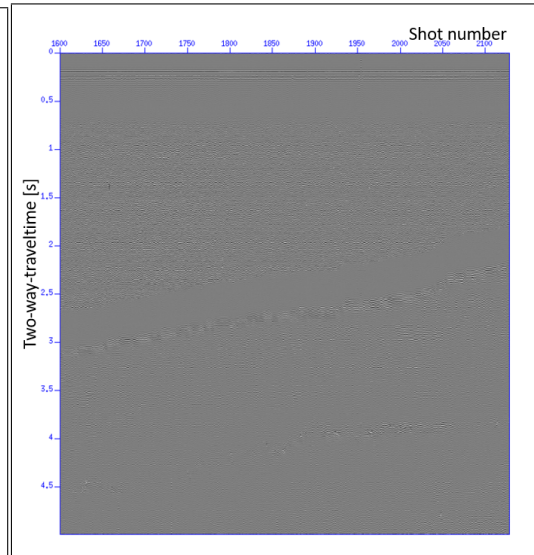


Figure 3.20: Zoom on common offset class 1 with filter 40-80-90-120 Hz.

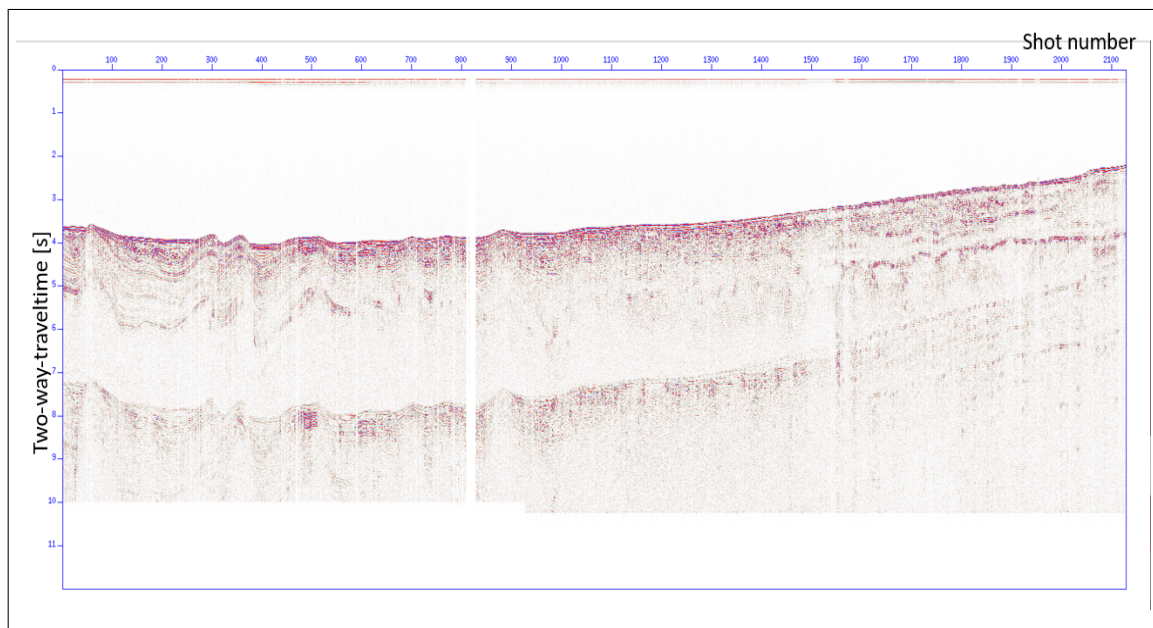


Figure 3.21: Common offset section for offset class 1, after the filtering process. This section is characterized by less noise.

The chosen value for the AGC time window length is 0.8 seconds. This time window length value has been chosen because it compensates the amplitude loss with depth at best. The final common offset section can be seen in **Figure 3.22**.

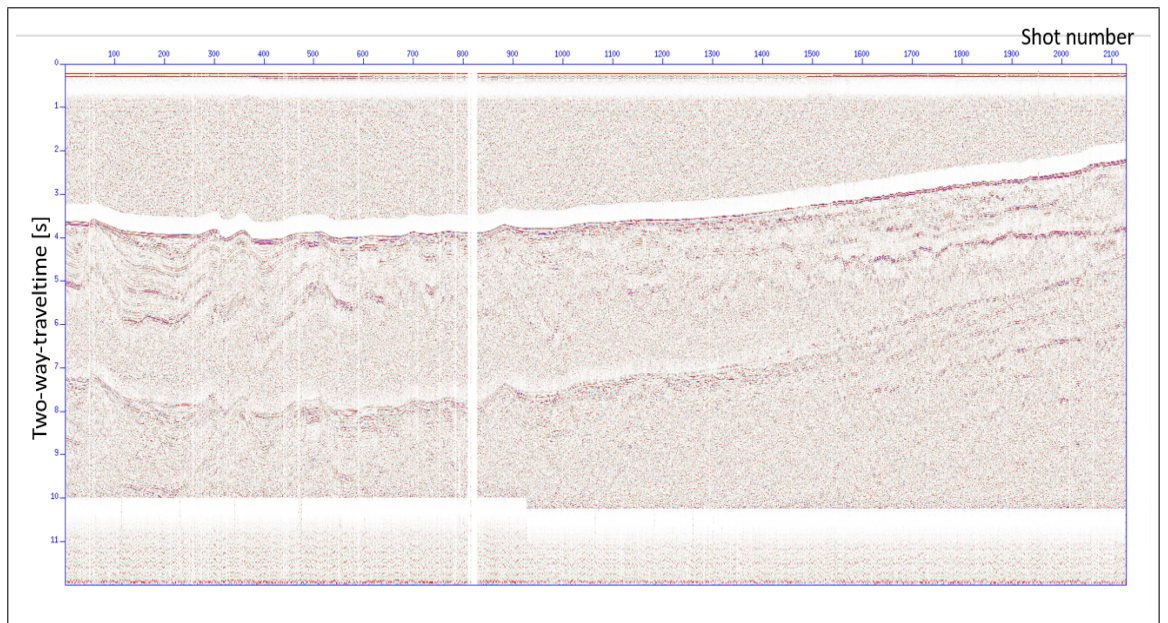


Figure 3.22: Common offset section for offset class 1, after the application of AGC.

3.6 Pre-stack time migration

The pre-stack time migration is an imaging technique used in order to migrate all the energy in its right subsurface position. The pre-stack time migration does not require a complex velocity model, but it can be applied on complex geological structures. In the first attempt, a pre-stack time migration with constant velocity equal to 1514 m/s (the velocity of the direct wave in water) has been performed. The pre-stack time migration has been applied to all offset classes (1-24) and then the results have been stacked together in order to obtain a migrated stack section. In **Figure 3.24** and in **Figure 3.25** there are the scripts used for the migration step. In the stack section obtained after this step, there are some artifacts caused by the constant velocity field used (smiles and wrong dips of the geological features in **Figure 3.23**).

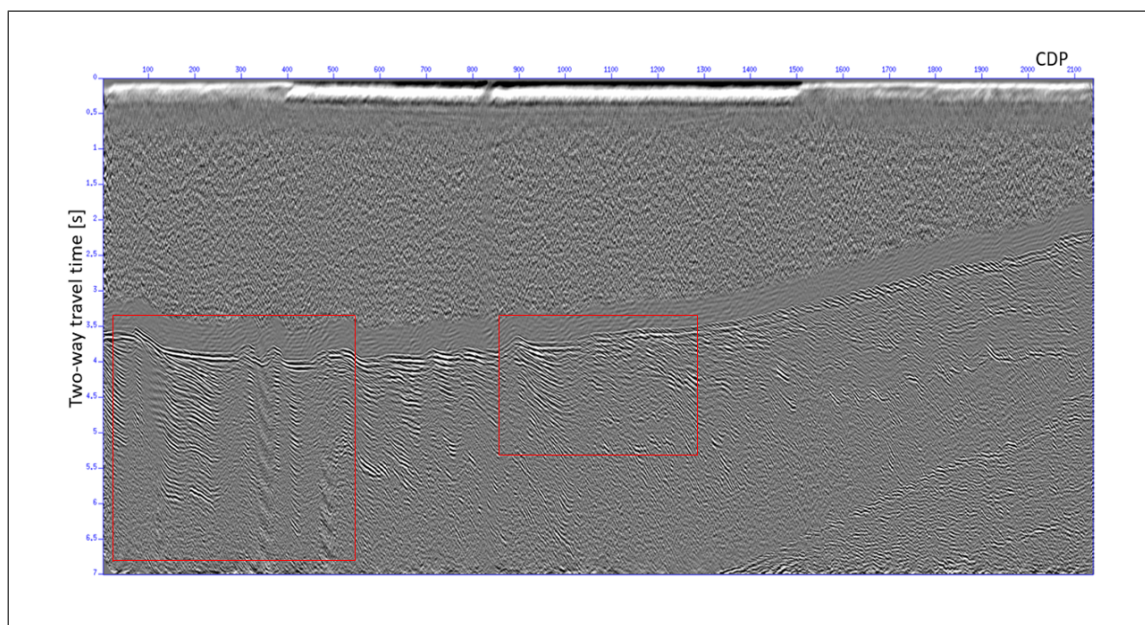


Figure 3.23: Migrated stack section with constant velocity (1514 m/s). In this section there are many artifacts (some of them are marked by red boxes).

The presence of these artifacts leads to consider a velocity field with a linear gradient with depth. This is necessary in order to migrate all the energy in its right subsurface position. Many tests with different values for the gradient have been carried out.

The physical law that connects velocity and time is the following one:

$$v = grad \cdot t + v_0 \quad (3.4)$$


```

suaddhead <vfilegrad3.bin ns=1751 | sushw key=dt a=4000 b=0 | sushw key=cdp a=1 b=1 >vrsnt.su

while [ $i -le $lasts ]
do
    off=`bc -l <<END
                (425+($i -1)*100)/2.
    END`

    suwind <zeroHea.su key=tracf min=$i max=$i | sushw key=offset,cdp,tracf a=0,1,0 b=0,1,0 > offset.su

    # choose the velocities with respect to the cdps in offset.su
    suwind <vrsnt.su key=cdp min=$k max=$j | sustrip >vcdp.bin

    echo "sto migrando offset"
    echo $off

    suktmig2d <offset.su vfile=vcdp.bin dx=100 verbose=1 angmax=60 hoffset=$off >>$fileo

    i=`expr $i + 1`
    j=`expr $j - 1`
    k=`expr $k - 1`

done

sustrip <ttt.su head=header >ttt
sustrip <$fileo | supaste ns=1751 head=header >ttt
mv ttt $fileo

susort <$fileo cdp offset | sustack | suximage perc=98 wbox=1800 hbox=800

exit

```

Figure 3.25: Second part of the script for the application of the pre-stack time migration process.

- gradient 2.0 (**Figure 3.44** and **Figure 3.45**)
- gradient 2.5 (**Figure 3.46** and **Figure 3.47**)
- gradient 3.0 (**Figure 3.48** and **Figure 3.49**).

After all the analysis made through the application of different gradients, it is visible that the velocity field must be composed by different gradients in different areas of the section. The best empirical velocity field is composed by (**Figure 3.50**):

- gradient 0.5 from CDP 0 to CDP 250;
- gradient 0.8 from CDP 250 to CDP 1450;
- gradient 1.2 from CDP 1450 to CDP 1800 ;
- gradient 2.0 from CDP 1800 to the end.

Before the application of the pre-stack time migration with the chosen velocity field, it was necessary to interpolate the shots in order to obtain a stack section without the spatial aliasing phenomenon. After the interpolation, the dataset was composed by a double number of shots and a better spatial

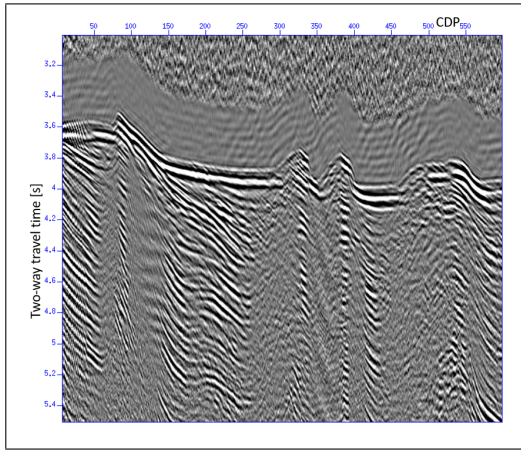


Figure 3.26: figure
Zoom 1 on stack section, migrated
with constant gradient.

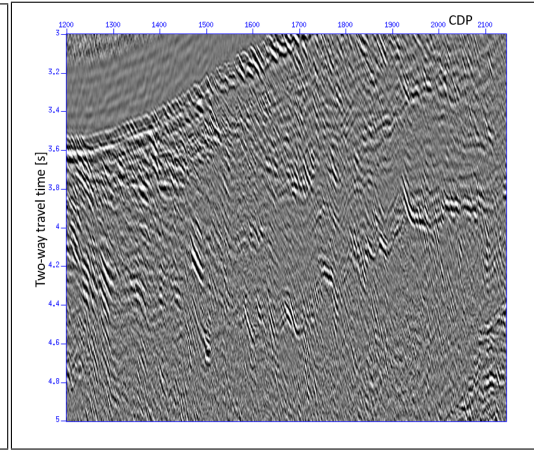


Figure 3.27: figure
Zoom 2 on stack section, migrated
with constant gradient.

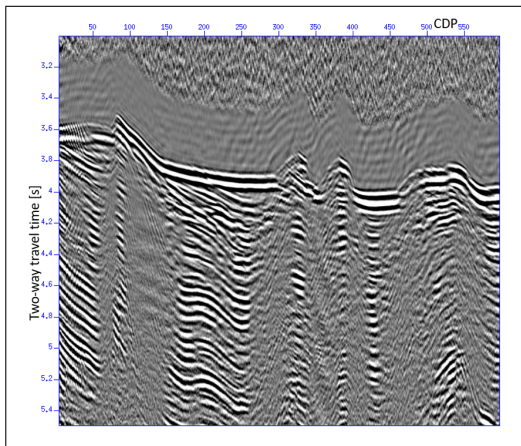


Figure 3.28: figure
Zoom 1 on stack section, migrated
with gradient 0.5.

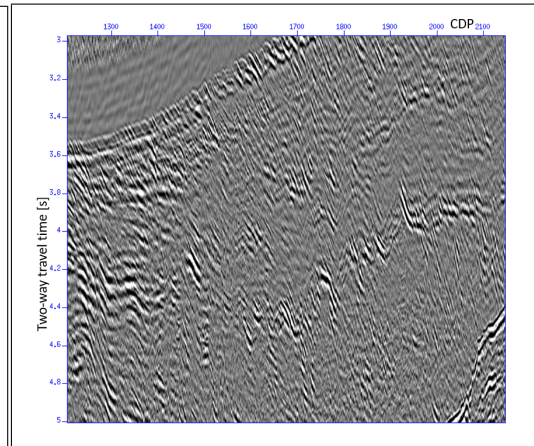


Figure 3.29: figure
Zoom 2 on stack section, migrated
with gradient 0.5.

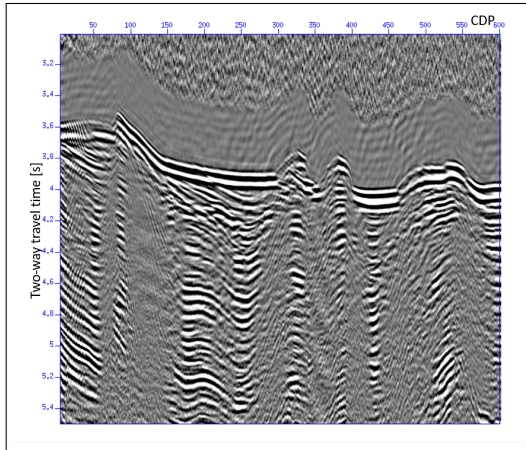


Figure 3.30: figure
Zoom 1 on stack section, migrated
with gradient 0.7.

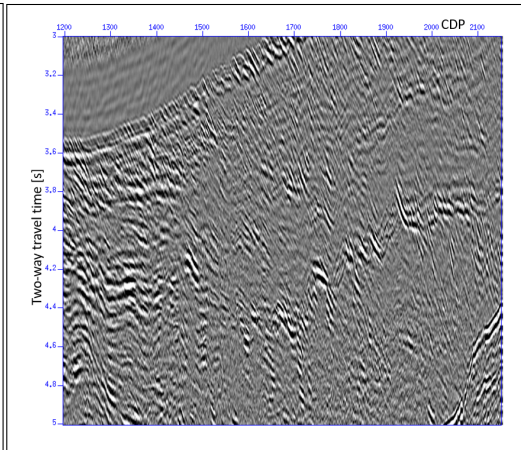


Figure 3.31: figure
Zoom 2 on stack section, migrated
with gradient 0.7.

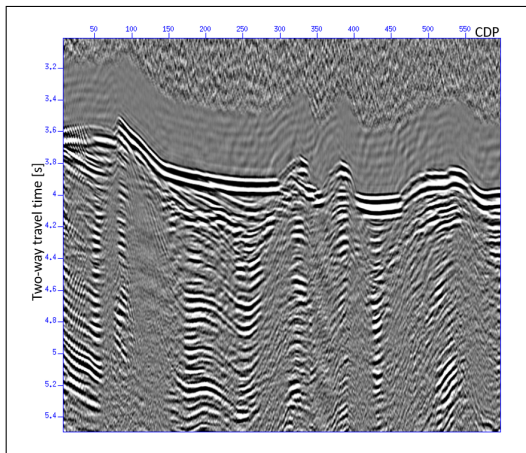


Figure 3.32: figure
Zoom 1 on stack section, migrated
with gradient 0.8.

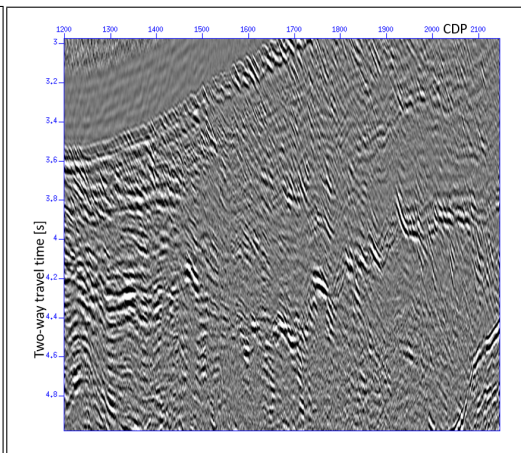


Figure 3.33: figure
Zoom 2 on stack section, migrated
with gradient 0.8.

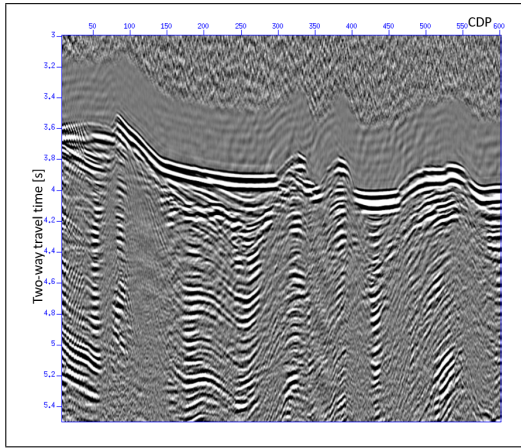


Figure 3.34: figure
Zoom 1 on stack section, migrated
with gradient 0.9.

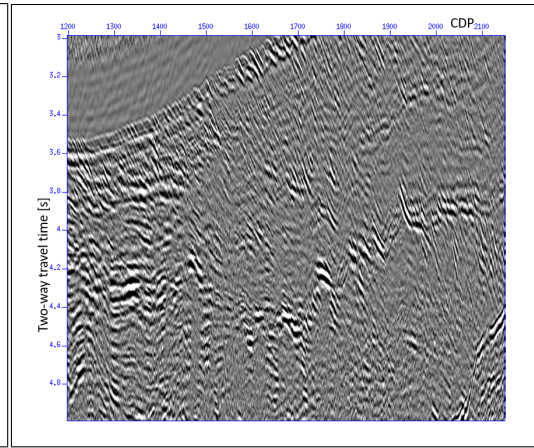


Figure 3.35: figure
Zoom 2 on stack section, migrated
with gradient 0.9.

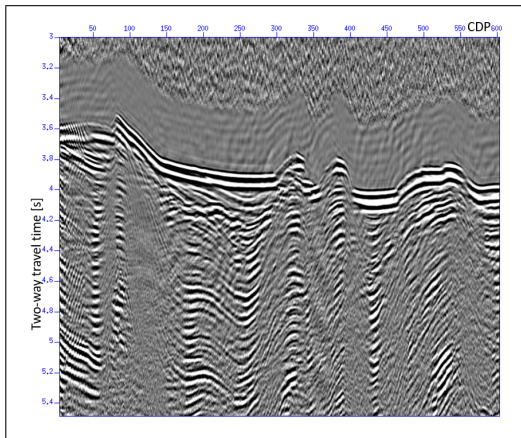


Figure 3.36: figure
Zoom 1 on stack section, migrated
with gradient 1.

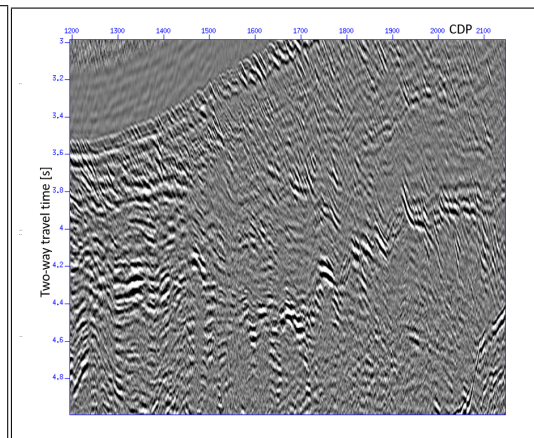


Figure 3.37: figure
Zoom 2 on stack section, migrated
with gradient 1.

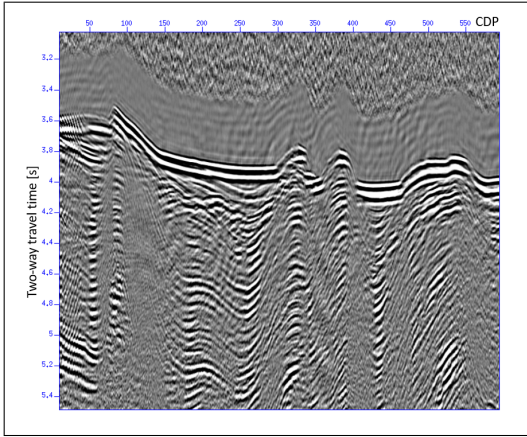


Figure 3.38: figure
Zoom 1 on stack section, migrated
with gradient 1.1.

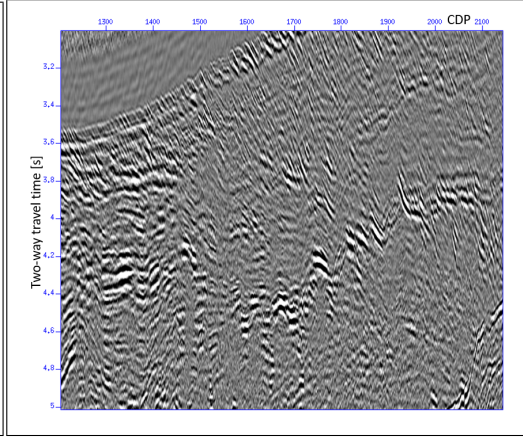


Figure 3.39: figure
Zoom 2 on stack section, migrated
with gradient 1.1.

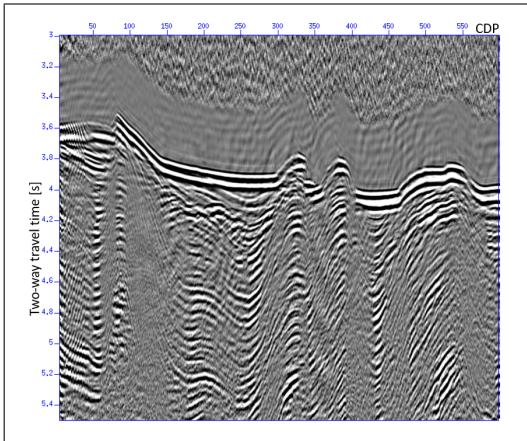


Figure 3.40: figure
Zoom 1 on stack section, migrated
with gradient 1.2.

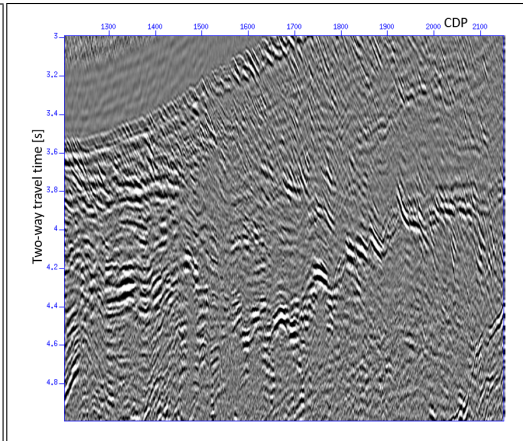


Figure 3.41: figure
Zoom 2 on stack section, migrated
with gradient 1.2.

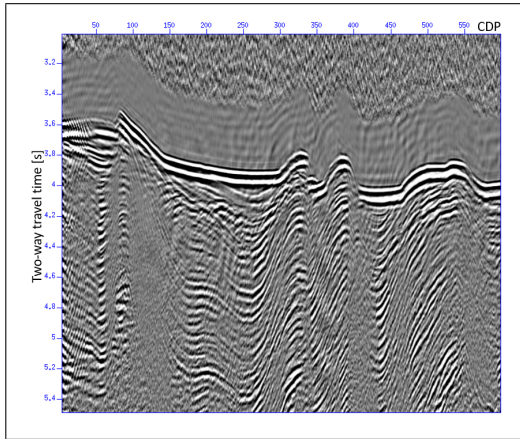


Figure 3.42: figure
Zoom 1 on stack section, migrated
with gradient 1.5.

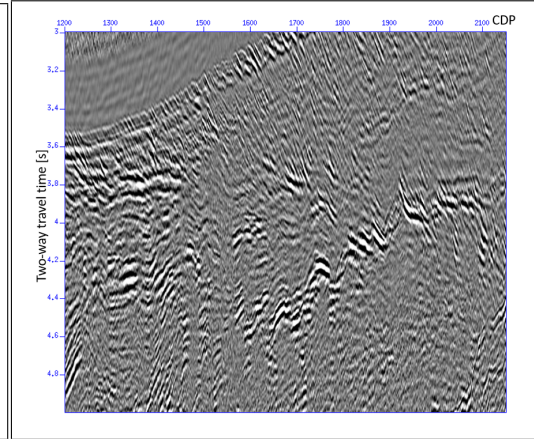


Figure 3.43: figure
Zoom 2 on stack section, migrated
with gradient 1.5.

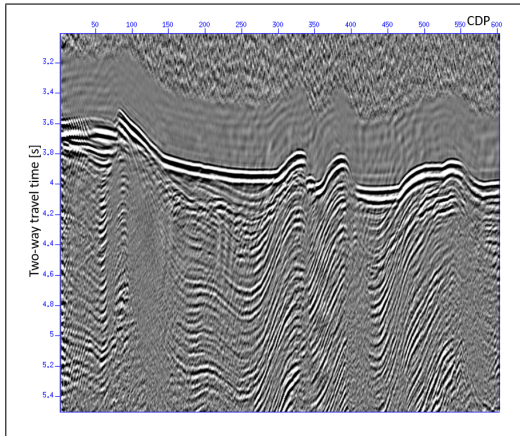


Figure 3.44: figure
Zoom 1 on stack section, migrated
with gradient 2.

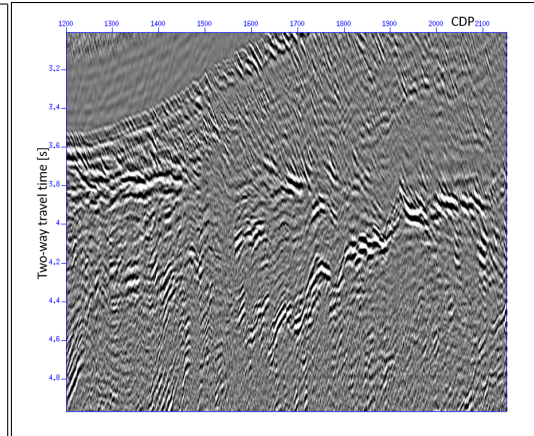


Figure 3.45: figure
Zoom 2 on stack section, migrated
with gradient 2.

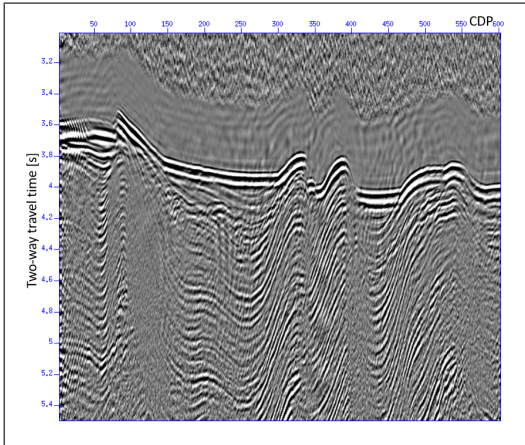


Figure 3.46: figure Zoom 1 on stack section, migrated with gradient 2.5.

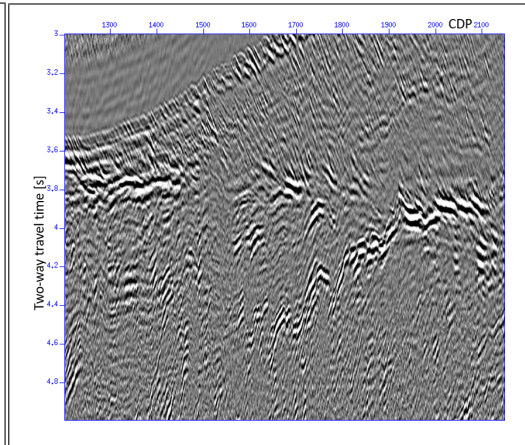


Figure 3.47: figure Zoom 2 on stack section, migrated with gradient 2.5.

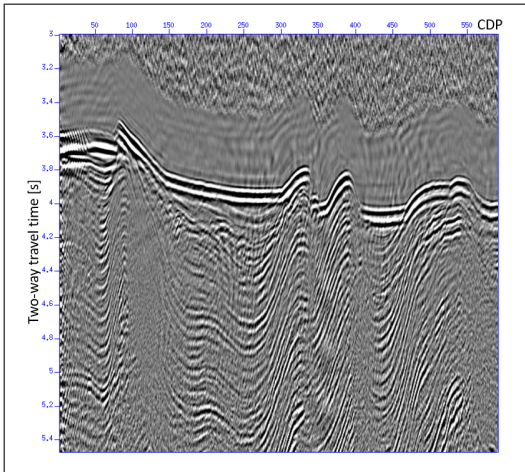


Figure 3.48: figure Zoom 1 on stack section, migrated with gradient 3.

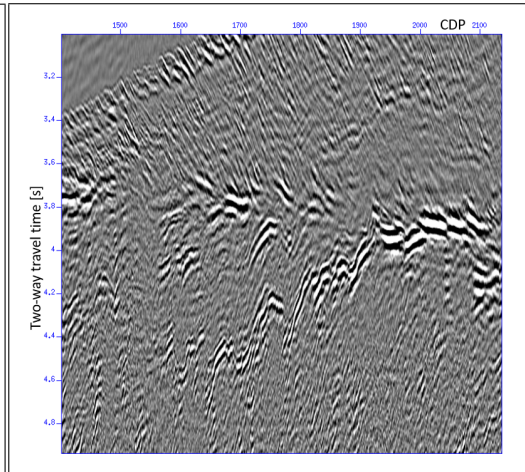


Figure 3.49: figure Zoom 2 on stack section, migrated with gradient 3.

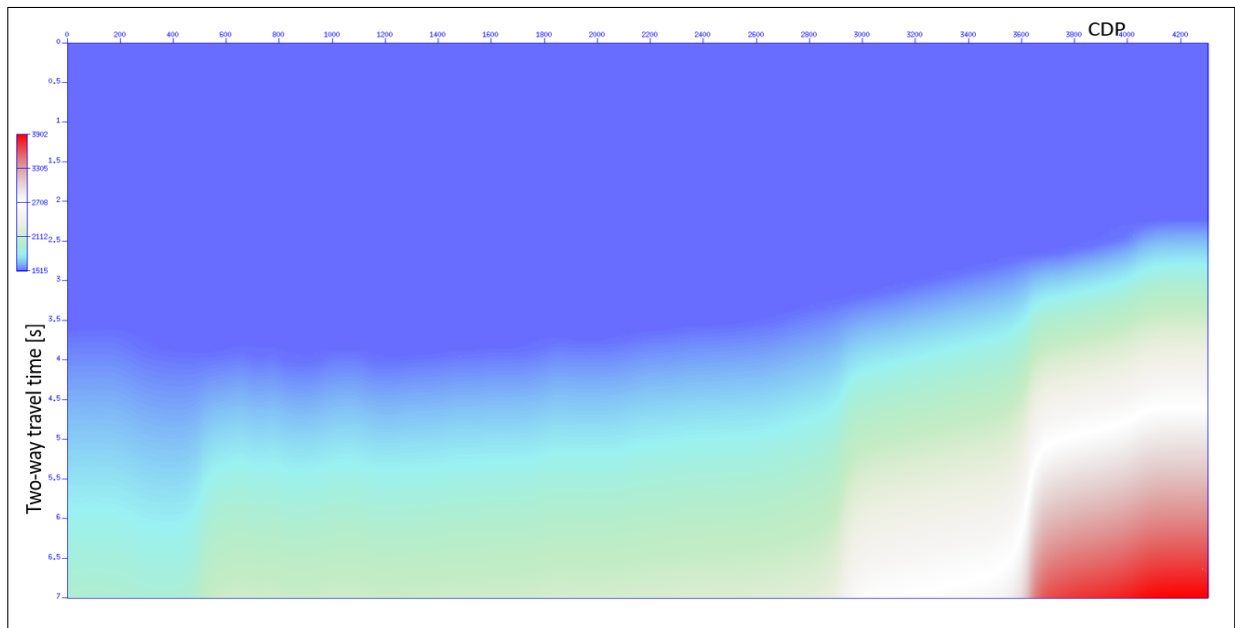


Figure 3.50: Plot 2D of the velocity field.

resolution. This new dataset required a new geometry due to the change in number of shots and the redefinition of the parameters for the migration (the script is shown in **Figure 3.51**).

```
sushw < MS052interp_tot.su key=ep a=1 b=1 c=0
j=4257 > tmp
susort < tmp ep tracf | sushw key=sx a=5000 b=0
c=50 j=24 | sushw key=offset a=-425 b=-100 c=0
j=24 | suchw key1=gx key2=offset key3=sx b=1 c=1
> MS052new_gwom_interp.su
sushw < MS052new_gwom_interp.su key=trac1 a=1
b=1 > MS052_final.su
```

Figure 3.51: Script used to set the new geometry after the interpolation process.

The migrated stack section has been obtained after the migration and the stacking processes, and it is shown in **Figure 3.52** .

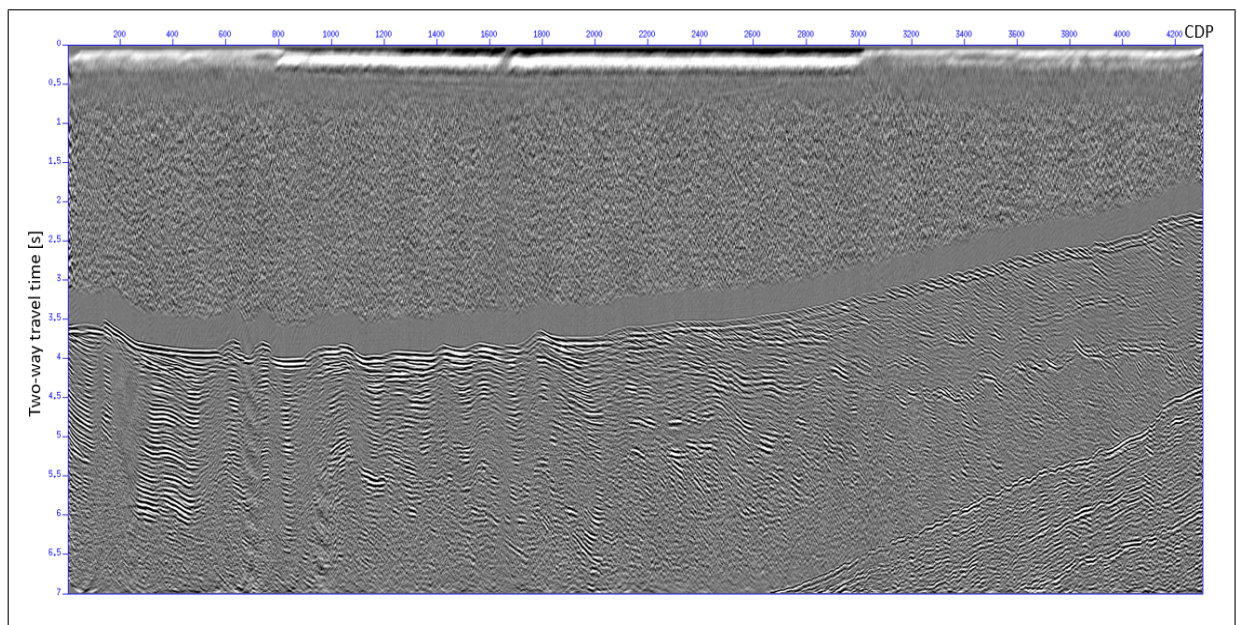


Figure 3.52: Stack section after the pre-stack time migration process using the 2D velocity field in **Figure 3.50**.

3.7 Post processing

Different steps have been applied after the migration process in order to remove all the remaining noise and to improve the quality of the final section. First of all, the filter described in the section 3.5 has been applied again to the data (script in **Figure 3.53**) that are the output of the migration step. **Figure 3.54** and **Figure 3.55** represent the common offset sections without the application of the filter and after the filtering process. Note how most of the high frequency noise generated by the migration has been removed.

```
sufilter < MS052_FINAL_PSTM.su f=3,6,90,120 >  
MS052_FINAL_PSTM_filtered.su
```

Figure 3.53: Script for the application of the filter characterized by the frequencies $f=3,6,90,120$ Hz.

Then, only the offset 1-10 have been maintained in the data because the last offset classes are characterized by a large amount of noise (**Figure 3.57**). So, the stacking process has been done only for the selected offsets. In **Figure 3.56**, it is possible to see the stack section with the selection of the offset classes 1-10.

After the stacking process, a narrower band-pass filter has been applied to the stacked data (**Figure 3.58**), in order to remove the highest frequencies. The filter is characterized by the frequencies 3,6,50,100 Hz (**Figure 3.59**). At the end, all the signal present above the sea floor has been removed with a muting process. The stack section after the muting process is visible in **Figure 3.60**. In this step, the picking of the sea floor done before has been used and all the signal above has been muted. **Figure 3.61** represents a zoom of the stack section after the muting process with the aim of clarifying if the interested reflector can be classified as a BSR or as a lithological reflector.

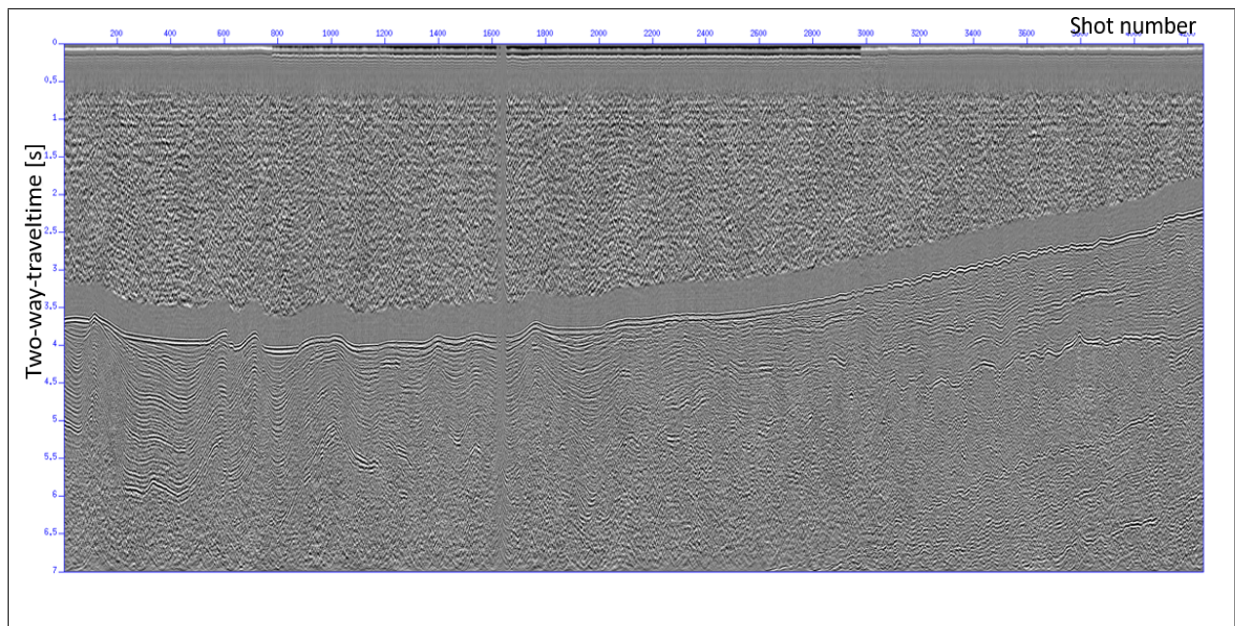


Figure 3.54: Common offset section for offset class 1 before the application of the filtering process.

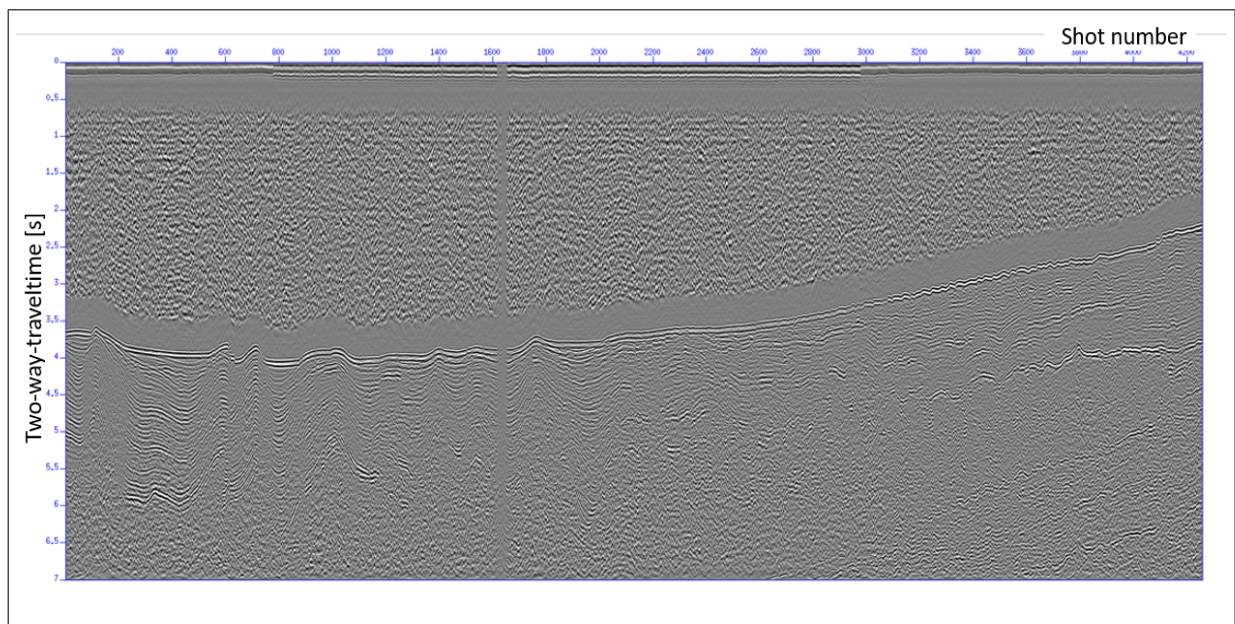


Figure 3.55: Common offset section for offset class 1 after the application of the filtering process. This section is characterized by less noise.

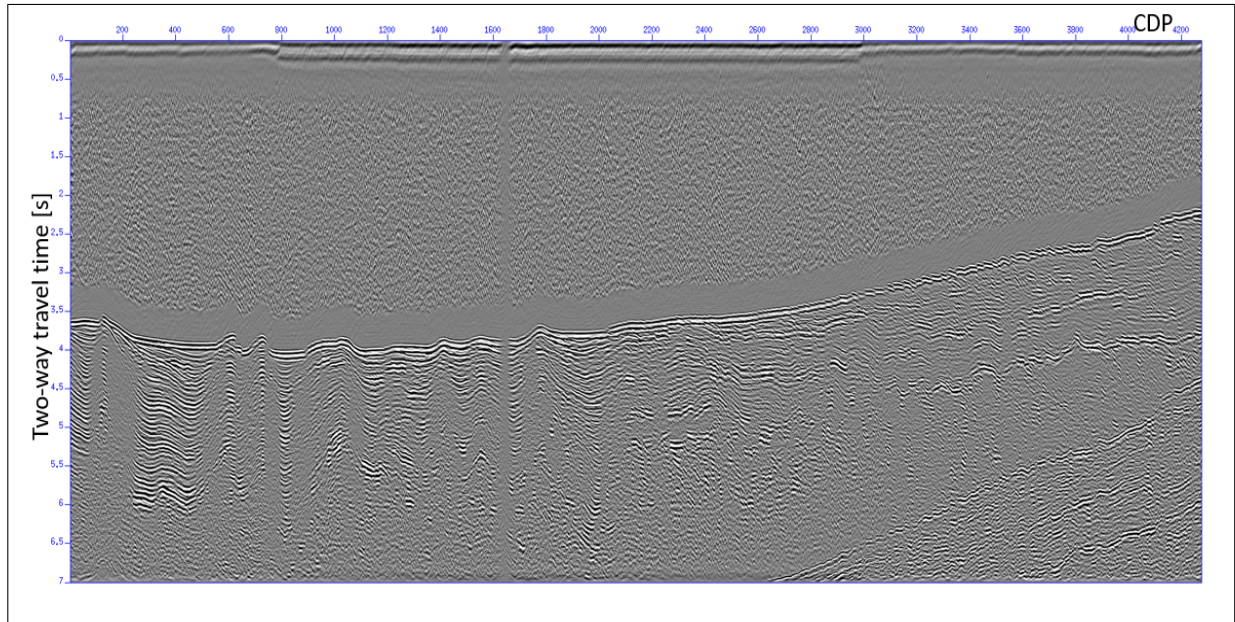


Figure 3.56: Migrated stack section with the selection of the offset classes 1-10. In this way, the artifacts due to the last offset classes have been deleted.

```
suwind < MS052_FINAL_PSTM_filtered.su key=tracf min=1  
max=10 > MS052_FINAL_PSTM_inparte.su  
susort < MS052_FINAL_PSTM_inparte.su cdp offset |  
sustack > MS052_FINAL_PSTM_stack.su
```

Figure 3.57: Script used for the selection of the traces 1-10, the sorting of the data and the stack process.

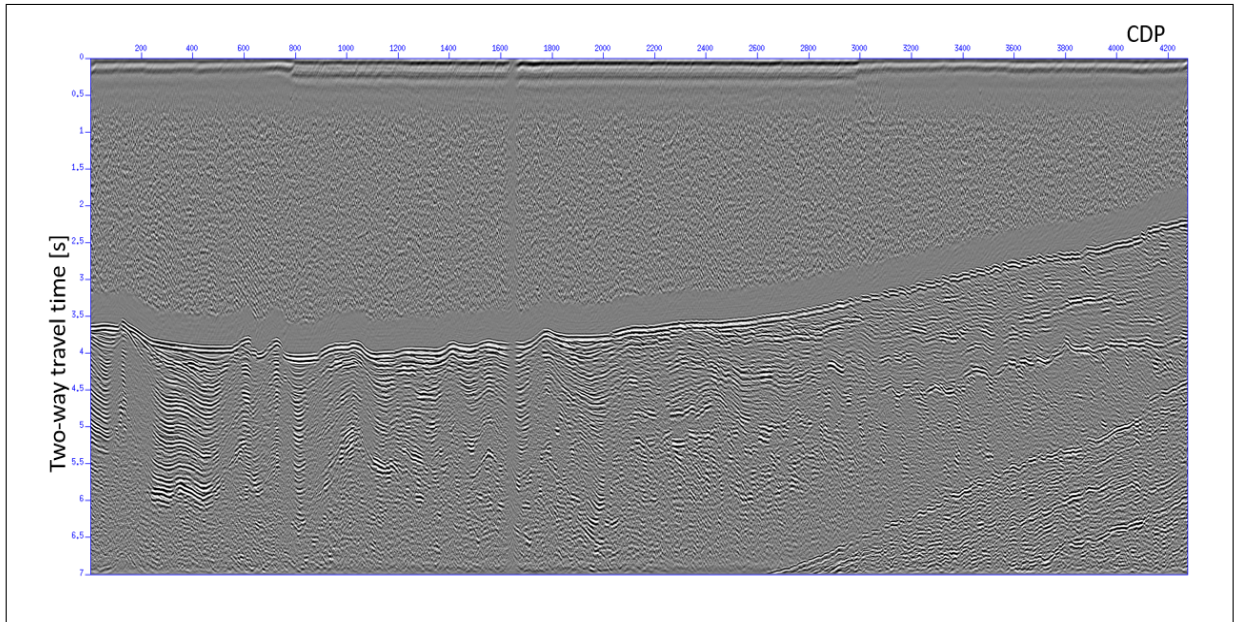


Figure 3.58: Migrated stack section with the application of the filter characterized by the frequencies $f=3,6,50,100$ Hz.

```
sufilter < MS052_FINAL_PSTM_stack.su f=3,6,50,100  
> MS052_FINAL_PSTM_filtrostretto.su
```

Figure 3.59: Script used for the application of the filter characterized by the frequencies 3,6,50,100 Hz.

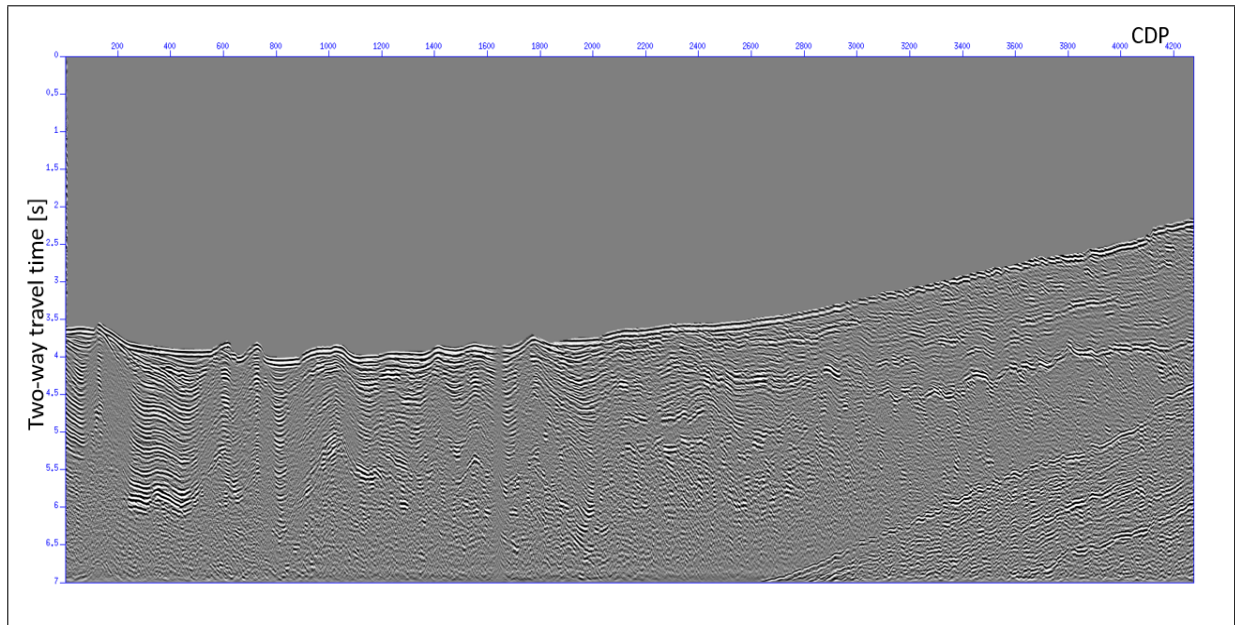


Figure 3.60: Migrated stack section after the application of the mute to the signal above the sea floor.

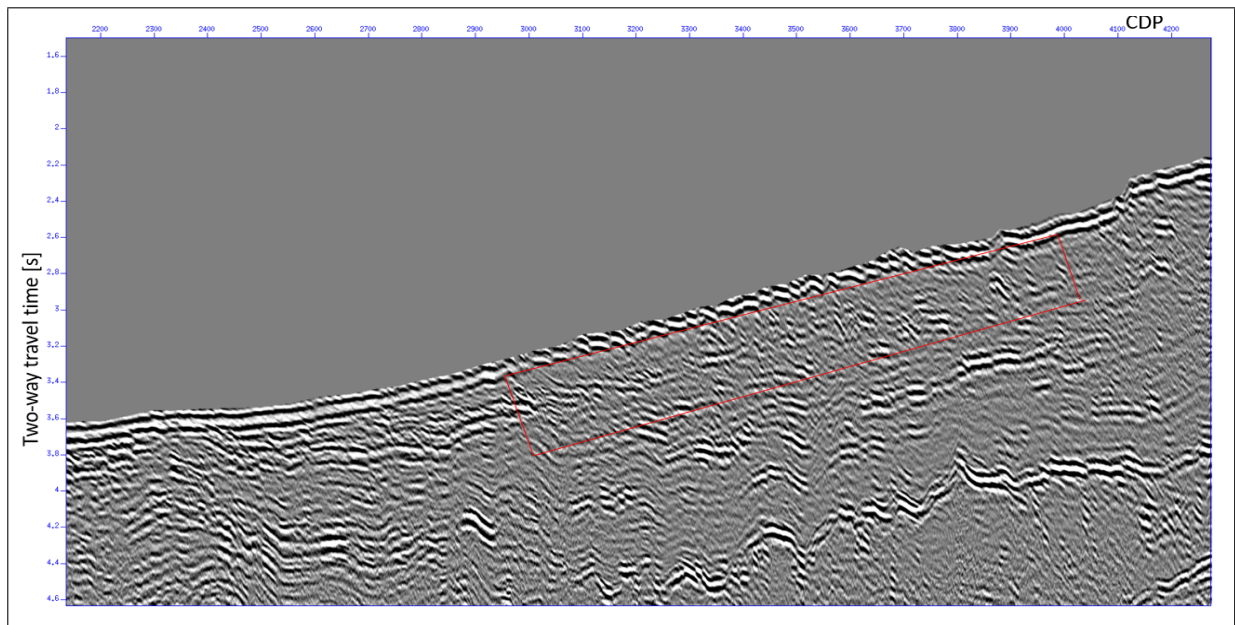


Figure 3.61: Zoom of the reflector that was defined by **Praeg et al. (2008)** as a BSR.

Chapter 4

Results

The processing carried out in this master thesis work has revealed that the BSR identified by **Praeg et al. (2008)** is actually a continuous lithological reflector (**Figure 3.61**). It cannot be defined as BRS because it is continuous, its shape is different from the one of the sea floor, and it does not present an inverse polarity with respect to the sea floor. This result does not imply that the MS-52 line area is characterized by the lack of gas hydrates. It is possible that gas hydrates are present in the area without showing a BSR, as in the cases described by **Majumdar et al. (2016)** and as in the case hypothesized by **Praeg et al (2022)**. However, the presence of gas hydrates is hampered by the particular conditions of salinity, temperature and water composition in the pores, as listed in **Camerlenghi et al. (2022)** article. In general, the Nile deep-sea fan is characterized by a large area, and the presence of gas hydrates in few places is defined (**Praeg et al. 2022**), but not in the region where the line MS-52 was acquired.

In the processing steps carried out in this work, a proper velocity analysis has not been carried out because an accurate analysis is very complex to develop with SU. At the same time, the target of the work was superficial and the whole interest was focused on the nature of that reflector (polarity and lithological continuity); these goals did not require a complex velocity model. This is also why a pre-stack time migration has been chosen. A possible extension of this processing consists in providing a detailed velocity field with the purpose of detecting other deeper lithological features that could point out the presence of gas hydrates.

Finally, this work was based on a dataset that was acquired 50 years ago, thus the technology of acquisition was less-advanced compared to today's equipment. The raw data of MS-52 line were pretty good, but the quality of the dataset has improved with the interpolation of the shots. After the interpolation process, the spatial aliasing is not anymore present in the sec-

tion. In this way, the spatial resolution improved, and also the quality of the stack section at the end of the processing. This work demonstrates how a good reprocessing can improve the quality of old data and allow a better geological interpretation.

APPENDIX A

After the processing, some preliminary analyses has been carried out in order to improve the accuracy of the velocity model derived from SU. This analyses required a specific software. For this work, the software Reveal has been used (<https://www.shearwatergeo.com/4/reveal-software>). This software has been created by Shearwater and it requires a license agreement. The 2D velocity model is obtained through picking of maxima on semblance panels, at several CDP locations along the seismic line. A semblance panel is a contour plot that is characterized by the velocity on the x-axis and the time on the y-axis. The goal is to create a function that peak all the maxima in the velocity-time plot. The semblance panel represents the coherency of the reflections in hyperbolic trajectories with different velocities. The velocity picking has been manually performed through an interactive window. In this interactive view there are different panels that should help the user in the picking process:

- the input CDP gather (panel 1 in **Figure 4.1**);
- the semblance panel, used to pick the maxima (panel 2 in **Figure 4.1**). In this panel, both the RMS and interval velocity profiles obtained after picking are shown in red;
- the CDP gather after Normal-Move-Out(NMO) correction with the new picked velocities (panel 3 in **Figure 4.1**). Ideally, all primary reflection after the correction should be flattened;
- the mini-stack section panel (stacked traces near the CDP location) (panel 4 in **Figure 4.1**);
- the navigation panel, with the location of the picked velocities along the line (panel 5 in **Figure 4.1**).

The correct velocity field has been determined by picking the maxima in the semblance panel for different CMPs positions. Between the CMPs positions

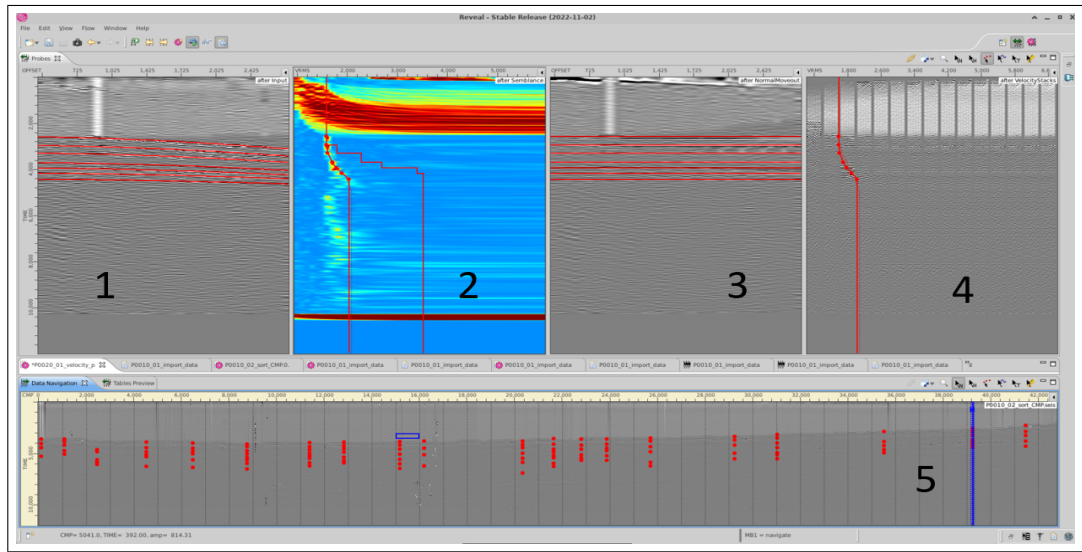


Figure 4.1: Velocity picking.

chosen, the interpolation is applied in order to obtain a continuous velocity model. In the semblance panels the maxima are constituted by the red regions. In this case, the upper part of the image is characterized by an extended red region that corresponds to the sea water. This area should not be considered in the velocity picking process. Below this area, it is possible to detect the maxima for the primary reflection below the sea bottom (the one that needs to be picked). Below these reflections, at times higher than 5 s approximately, another similar region develops, characterized by lower velocities. This area corresponds to the multiples, so it should not be considered for the velocity analysis. However, due to the shallow target of our investigation, velocities in the multiple regions are not of interest for this study.

After the velocity picking process, a 2D velocity model is obtained, where the different values of velocity are plotted in different regions (**Figure 4.2**). The red dots are the CDP locations where the velocity picking has been performed. The time-axis in the plot goes from 0 to 7 seconds (as in the plot 2D of the velocity field made with SU), and the velocity scale goes from 1515 m/s to 3900 m/s. The 2D velocity plot shows 2 areas characterized by higher velocities (between the CDPs 6000 and 8000 and between the CDPs 26000 and 30000).

The picking process described above is an alternative way to retrieve the 2D velocity model for migration, with respect to the empirical method used in this thesis. It could improve the accuracy of the velocity model and lead to

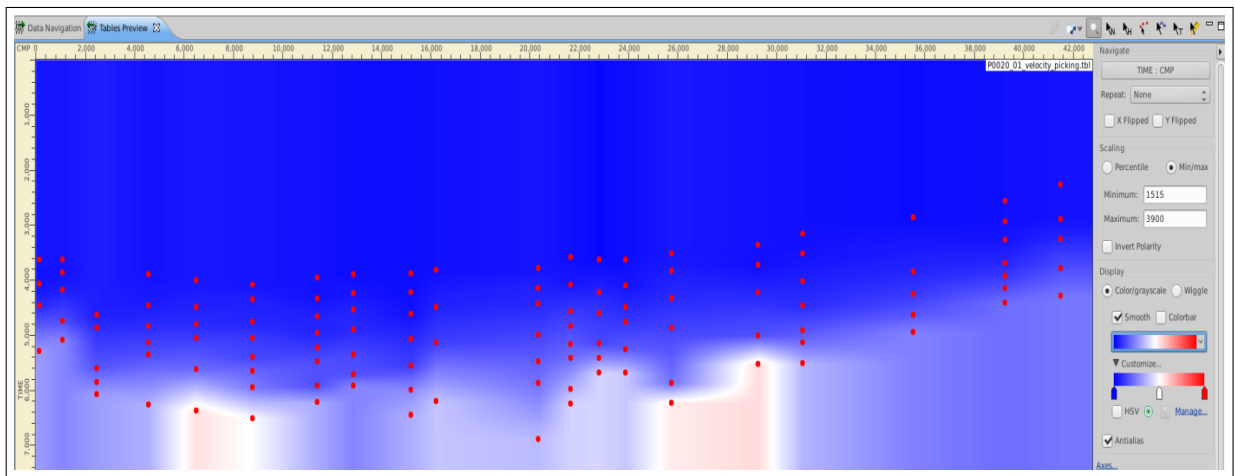


Figure 4.2: Plot 2D of the velocity field made with Reveal.

a migrated stack section that is more precise and with less artifacts. The main disadvantage of this procedure is the need of a specific software, and the need for an expert user able to recognize and avoid picking the multiples.

References

- [Schicks 2022]** Schicks, J.M. (2022) "Gas hydrates in nature and in the laboratory: necessary requirements for formation and properties of the resulting hydrate phase", ChemTexts(Cham). Cham: Springer International Publishing, 8(2), pp. 1-10. doi: 10.1007/s40828-022-00164-3.
- [Majid and Koh 2021]** Majid, A.A.A., & Koh, A.C. (2021) '8 - Self-preservation phenomenon in gas hydrates and its application for energy storage' In: Bernstein, E. (ed.) 'Intra- and Intermolecular Interactions Between Non-covalently Bonded Species'. Elsevier, pp. 267-285.
- [Cook and Portnov 2022]** Cook, A.E., & Portnov, A. (2022) 'Natural gas hydrates' In: Bell, R., Iacopini, D., Vardy, M. (eds.) 'Interpreting Subsurface Seismic Data'. Elsevier, pp. 17-32.
- [Praeg et al 2008]** Praeg, D., Geletti, R., Mascle, J., Unnithan, V., & Harmegnies, F. (2008) Geophysical exploration for gas hydrates in the Mediterranean Sea and a bottom simulating reflection on the Nile fan. GNGTS 2008, Session 3.2.
- [Camerlenghi et al 2022]** Camerlenghi, A., & Corradin, C., & Tinivella, U., & Giustiniani, M., & Bertoni, C. (2022) Subsurface heat and salts cause exceptionally limited methane hydrate stability in the Mediterranean Basin. Geological Society of America. 51(2), 162-166.
- [Merey and Longinos 2018]** Merey, S., & Longinos, S. N. (2018) Does the Mediterranean Sea have potential for producing gas hydrates? J Natural Gas Sci Eng 55, 113-134.
- [Mordis et al. 2019]** Mordis, G.J., & Collet, T.S., & Boswell, R., & Kurihara, M., & Reagan, M.T., & Koh, C., & Sloan, E.D. (2019) Toward production from gas hydrates: current status, assessment of resources, and simulation based evaluation of technology and potential. SPE Reservoir Evaluation Engineer. 12(5):745-771.
- [Boswell et al. 2017]** Boswell, R., & Schoderbek, D., & Collett, T.S., & Ohtsuki, S., & White, M.D., & Anderson, B.J. (2017) The Ignik Sikumi

field experiment, Alaska north slope: design, operations, and implications for CO₂-CH₄ exchange in gas hydrate reservoirs. *Energy Fuel*. 31(1):140–153.

[Obhodas et al. 2019] Obhodas, J., & Tinivella, U., & Giustiniani, M., & Durn, T., & Vinkovic, A., & Radic, S., & Soprun, F., & Sudac, D. (2019) Past and present potential of the Adriatic deep sea sediments to produce methane hydrates. *Journal of Soils and Sediments* (2020). 20:2724–2732.

[Lykousis et al. 2009] Lykousis, V., Alexandri, S., Woodside, J., de Lange, G., Dählmann, A., Perissoratis, C., Heeschen, K., Ioakim, Chr., Sakellariou, D., Nomikou, P., Rousakis, G., Casas, D., Ballas, D. & Ercilla, G. (2009) Mud volcanoes and gas hydrates in the Anaximander mountains (Eastern Mediterranean Sea). *Marine and Petroleum Geology*. 26(6), 854-872.

[Majumdar et al. 2016] Majumdar, U., Cook, A. E., Shedd, W. & Frye, M. (2016) The connection between natural gas hydrate and bottom-simulating reflectors. *Geophysical Research Letters*. 43, 7044–7051. doi:10.1002/2016GL069443.

[Praeg et al. 2022] Praeg, D., Migeon, S., Mascle, J., Unnithan, V. & Ketzer, M. (2022) A Gas Hydrate System of Heterogeneous Character in the Nile Deep-Sea Fan. In: Mienert, J., Berndt, C., Tréhu, A.M., Camerlenghi, A. & Liu CS. (eds.) *World Atlas of Submarine Gas Hydrates in Continental Margins*, Springer. 437-447.

[Cohen et al., 2023] Cohen, J. K. and Stockwell, Jr. J. W., (2023), CWP/SU: Seismic Unix Release No. SU44R28: an open source software package for seismic research and processing, Center for Wave Phenomena, Colorado School of Mines.

List of figures

Figure 1.1: Main types of polyhedra: structures I, II and H. Schicks, J.M. (2022) 'Gas hydrates in nature and in the laboratory: necessary requirements for formation and properties of the resulting hydrate phase', Chem-Texts(Cham). Cham: Springer International Publishing, 8(2), pp. 1-10. doi: 10.1007/s40828-022-00164-3.

Figure 1.2: Example of the stability zone for methane hydrate, which depends on the depth and temperature. Cook, A.E., & Portnov, A. (2022) 'Natural gas hydrates' In: Bell, R., Iacopini, D., Vardy, M. (eds.) 'Interpreting Subsurface Seismic Data'. Elsevier, pp. 17-32.

Figure 1.3: Examples of different types of BSRs. Cook, A.E., & Portnov, A. (2022) 'Natural gas hydrates' In: Bell, R., Iacopini, D., Vardy, M. (eds.) 'Interpreting Subsurface Seismic Data'. Elsevier, pp. 17-32.

Figure 1.4 Reprocessed stack section of MS52 line. Praeg, D., Geletti, R., Mascle, J., Unnithan, V., & Harmegnies, F., (2008). Geophysical exploration for gas hydrates in the Mediterranean Sea and a bottom simulating reflection on the Nile fan. GNGTS 2008, Session 3.2.

Figure ?? Zoom of a region in the stack section characterized by the BSR. Praeg, D., Geletti, R., Mascle, J., Unnithan, V., & Harmegnies, F., (2008). Geophysical exploration for gas hydrates in the Mediterranean Sea and a bottom simulating reflection on the Nile fan. GNGTS 2008, Session 3.2.

Figure 1.5 Bathymetric map with the location of the MS-52 line, the exploration wells Kg45-1 and Kg49-1 and 2D and 3D seismic exploration. Praeg, D., Migeon, S., Mascle, J., Unnithan, V. & Ketzer, M. (2022) A Gas Hydrate System of Heterogeneous Character in the Nile Deep-Sea Fan. In: Mienert, J., Berndt, C., Tréhu, A.M., Camerlenghi, A. & Liu CS. (eds.) World Atlas of Submarine Gas Hydrates in Continental Margins, Springer. 437-447.

Figure 1.6 Identification of BSRs in 3D and 2D seismic profiles in the Praeg et al. article (2022). Praeg, D., Migeon, S., Mascle, J., Unnithan, V. & Ketzer, M. (2022) A Gas Hydrate System of Heterogeneous Character in the

Nile Deep-Sea Fan. In: Mienert, J., Berndt, C., Tréhu, A.M., Camerlenghi, A. & Liu CS. (eds.) World Atlas of Submarine Gas Hydrates in Continental Margins, Springer. 437-447.

Figure 2.1 Position of the line MS52. Praeg, D., Geletti, R., Mascle, J., Unnithan, V., & Harmegnies, F., (2008). Geophysical exploration for gas hydrates in the Mediterranean Sea and a bottom simulating reflection on the Nile fan. GNGTS 2008, Session 3.2.

Figure 2.2 This figure represents the scheme of acquisition. In particular, two consecutive shots are visible (red stars) with the relative hydrophones (blue triangles). The spacing between two consecutive shots is 100 meters, and it is equal to the spacing between two hydrophones.

Figure 2.3 Example of a shot gather with 24 channels.

Figure 3.1 SU script used for the addition of 13 traces with zero amplitude.

Figure 3.2 Script to set the geometry.

Figure 3.3 Common offset section for offset class 1 after the geometry assignment. In this figure a multiple can be identified.

Figure 3.4 Script for noise removal.

Figure 3.5 Example of a shot gather characterized by noisy spikes.

Figure 3.6 Example of a shot gather characterized by a cut below 4.8 s two-way-traveltime.

Figure 3.7 Example of a shot gather characterized by swell noise.

Figure 3.8 Common offset section for offset class 1, after the noise removal. In this section, it is possible to see where most of the traces have been set to zero. The section after the noise removal process presents clearer geological characteristics.

Figure 3.9 Script for the spherical divergence correction.

Figure 3.10 Common offset section for offset class 1, after the spherical divergence correction. After this step, the amplitude has been restored in depth. The multiple is more visible.

Figure 3.11 Zoom on common offset class 1 with filter 3-6-10-20 Hz.

Figure 3.12 Zoom on common offset class 1 with filter 3-6-16-32 Hz.

Figure 3.13 Zoom on common offset class 1 with filter 5-10-20-40 Hz.

Figure 3.14 Zoom on common offset class 1 with filter 10-20-30-60 Hz.

Figure 3.15 Zoom on common offset class 1 with filter 15-30-40-80 Hz.

Figure 3.16 Zoom on common offset class 1 with filter 20-40-50-100 Hz.

Figure 3.17 Zoom on common offset class 1 with filter 25-50-60-120 Hz.

Figure 3.18 Zoom on common offset class 1 with filter 30-60-70-120 Hz.

Figure 3.19 Zoom on common offset class 1 with filter 35-70-80-120 Hz.

Figure 3.20 Zoom on common offset class 1 with filter 40-80-90-120 Hz.

Figure 3.21 Common offset section for offset class 1, after the filtering process. This section is characterized by less noise.

Figure 3.22 Common offset section for offset class 1, after the application of AGC.

Figure 3.23 Migrated stack section with constant velocity (1514 m/s). In this section there are many artifacts (some of them are marked by red boxes).

Figure 3.24 First part of the script for the application of the pre-stack time migration process.

Figure 3.25 Second part of the script for the application of the pre-stack time migration process.

Figure 3.26 Zoom 1 on stack section, migrated with constant gradient.

Figure 3.27 Zoom 2 on stack section, migrated with constant gradient.

Figure 3.28 Zoom 1 on stack section, migrated with gradient 0.5.

Figure 3.29 Zoom 2 on stack section, migrated with gradient 0.5.

Figure 3.30 Zoom 1 on stack section, migrated with gradient 0.7.

Figure 3.31 Zoom 2 on stack section, migrated with gradient 0.7.

Figure 3.32 Zoom 1 on stack section, migrated with gradient 0.8.

Figure 3.33 Zoom 2 on stack section, migrated with gradient 0.8.

Figure 3.34 Zoom 1 on stack section, migrated with gradient 0.9.

Figure 3.35 Zoom 2 on stack section, migrated with gradient 0.9.

Figure 3.36 Zoom 1 on stack section, migrated with gradient 1.

Figure 3.37 Zoom 2 on stack section, migrated with gradient 1.

Figure 3.38 Zoom 1 on stack section, migrated with gradient 1.1.

Figure 3.39 Zoom 2 on stack section, migrated with gradient 1.1.

Figure 3.40 Zoom 1 on stack section, migrated with gradient 1.2.

Figure 3.41 Zoom 2 on stack section, migrated with gradient 1.2.

Figure 3.42 Zoom 1 on stack section, migrated with gradient 1.5.

Figure 3.43 Zoom 2 on stack section, migrated with gradient 1.5.

Figure 3.44 Zoom 1 on stack section, migrated with gradient 2.

Figure 3.45 Zoom 2 on stack section, migrated with gradient 2.

Figure 3.46 Zoom 1 on stack section, migrated with gradient 2.5.

Figure 3.47 Zoom 2 on stack section, migrated with gradient 2.5.

Figure 3.48 Zoom 1 on stack section, migrated with gradient 3.

Figure 3.49 Zoom 2 on stack section, migrated with gradient 3.

Figure 3.50 Plot 2D of the velocity field.

Figure 3.51 Script used to set the new geometry after the interpolation process.

Figure 3.52 Stack section after the pre-stack time migration process using the 2D velocity field in **Figure 3.50**.

Figure 3.53 Script for the application of the filter characterized by the frequencies $f=3,6,90,120$ Hz.

Figure 3.54 Common offset section for offset 1 before the application of the filtering process.

Figure 3.55 Common offset section for offset class 1 after the application of the filtering process. This section is characterized by less noise.

Figure 3.56 Migrated stack section with the selection of the offset classes 1-10. In this way, the artifacts due to the last offset classes have been deleted.

Figure 3.57 Script used for the selection of the traces 1-10, the sorting of the data and the stack process.

Figure 3.58 Migrated stack section with the application of the filter characterized by the frequencies $f=3,6,50,100$ Hz.

Figure 3.59 Script used for the application of the filter characterized by the frequencies 3,6,50,100 Hz.

Figure 3.60 Migrated stack section after the application of the mute to the signal above the sea floor.

Figure 3.61 Zoom of the reflector that was defined by **Praeg et al. (2008)** as a BSR.

Figure 4.1 Velocity picking.

Figure 4.2 Plot 2D of the velocity field made with Reveal.